

# Supernova Resonance-scattering Line Profiles in the Absence of a Photosphere

Brian Friesen<sup>1</sup>, E. Baron<sup>1,2,3,4</sup>, David Branch<sup>1</sup>, Bin Chen<sup>1</sup>, Jerod T. Parrent<sup>5,6</sup>, and  
R. C. Thomas<sup>3</sup>

## ABSTRACT

In supernova spectroscopy relatively little attention has been given to the properties of optically thick spectral lines in epochs following the photosphere’s recession. Most treatments and analyses of post-photospheric optical spectra of supernovae assume that forbidden-line emission comprises most if not all spectral features. However, evidence exists which suggests that some spectra exhibit line profiles formed via optically thick resonance-scattering even months or years after the supernova explosion. To explore this possibility we present a geometrical approach to supernova spectrum formation based on the “Elementary Supernova” model, wherein we investigate the characteristics of resonance-scattering in optically thick lines while replacing the photosphere with a transparent central core emitting non-blackbody continuum radiation, akin to the optical continuum provided by decaying  $^{56}\text{Co}$  formed during the explosion. We develop the mathematical framework necessary for solving the radiative transfer equation under these conditions, and calculate spectra for both isolated and blended lines. Our comparisons with analogous results from the Elementary Supernova code **SYNOW** reveal several marked differences in line formation. Most notably, resonance lines in these conditions form P Cygni-like profiles, but the emission peaks and absorption troughs shift redward and blueward, respectively, from the line’s rest wavelength by a significant amount, despite the spherically symmetric distribution of the line optical depth in the ejecta. These properties and others that we find in this work could lead to misidentification of lines or misattribution of properties of line-forming material at post-photospheric times in supernova optical spectra.

---

<sup>1</sup>Homer L. Dodge Department of Physics & Astronomy, University of Oklahoma, 440 W. Brooks St., Rm. 100, Norman, OK 73019, USA

<sup>2</sup>Hamburger Sternwarte, Gojenbergsweg 112, 21029 Hamburg, Germany

<sup>3</sup>Computational Cosmology Center, Computational Research Division, Lawrence Berkeley National Laboratory, MS 50B-4206, 1 Cyclotron Road, CA 94720, USA

<sup>4</sup>Department of Physics, University of California, Berkeley, CA 94720, USA

<sup>5</sup>6127 Wilder Lab, Department of Physics & Astronomy, Dartmouth College, Hanover, NH 03755, USA

<sup>6</sup>Las Cumbres Observatory Global Telescope Network, Goleta, CA 93117, USA

## 1. Introduction

Many of the physical processes which contribute to spectrum formation in a supernova (SN) change dramatically as it ages. Given the difficulty and complexity of including all such processes, as well as their evolution in time, exploration into this computational frontier has begun only very recently (Pinto & Eastman 2000; Höflich 2003; Kasen et al. 2006; Jack et al. 2009; Kromer & Sim 2009; De et al. 2010; Dessart & Hillier 2010, 2011; Hillier & Dessart 2012). Most work in SN spectroscopy has focused on the early “photospheric” phase, comprising the time from explosion to a few weeks post-maximum light, where resonance-scattering from permitted lines dominates the spectrum (Branch et al. 1983, 1985; Jeffery et al. 1992; Mazzali & Lucy 1993; Mazzali et al. 1995; Fisher et al. 1997; Mazzali et al. 1997; Hatano et al. 1999a; Mazzali 2000, 2001; Branch et al. 2005; Dessart & Hillier 2005; Mazzali et al. 2005; Hachinger et al. 2006). Considerably less attention has been given to the “nebular” phase, several months or more after explosion, where emission from forbidden lines constitute most of the spectrum (Axelrod 1980; Ruiz-Lapuente & Lucy 1992; Kozma & Fransson 1998a,b; Mazzali et al. 1998; Maeda et al. 2006; Jerkstrand et al. 2011; Mazzali et al. 2011). Finally, the intermediate phases, that is, a few months post-explosion, have received the least amount of scrutiny (Maurer et al. 2011). One reason so much attention focuses on either very early or very late times is that in these regimes one can reproduce with reasonable fidelity the physical processes which dominate spectrum formation through a number of simplifying assumptions. For example, in the early, photospheric phase the Sobolev approximation (Castor 1970) and a resonance-scattering source function (Jeffery & Branch 1990) are both accurate approximations due to the high densities and steep velocity gradients in the SN ejecta; at late times one typically assumes both that the ejecta is optically thin and that line emission arises exclusively from forbidden lines (Axelrod 1980). However these two groups of assumptions are generally incompatible with each other in the intermediate regime of a SN.

Complicating matters further is the possibility that the evolution of the different types of line-forming processes is asynchronous. Specifically, the emergence of forbidden emission lines in a SN spectrum may not herald the systematic withdrawal of resonance-scattering in optically thick permitted lines. Though this possibility has frequently been acknowledged (Bowers et al. 1997; Branch et al. 2005; Jerkstrand et al. 2011), it has to our knowledge never been pursued in detail until now. To illustrate this point we show in Figures 1 and 2 **SYNOW** fits to the day +87 optical spectrum of SN 2003du and the day +115 spectrum of SN 1994D, respectively. In the SN 2003du fit we use only three ions: Na I, Ca II and Fe II. The photospheric velocity is  $7000 \text{ km s}^{-1}$ , and the photospheric temperature is 8000 K. The excitation temperatures of all three ions is 7000 K. In the SN 1994D fit, we include five ions: Na I, Ca II, Cr II, Fe II, and Co II. Here the photospheric velocity is  $6000 \text{ km s}^{-1}$  and the temperature is 10,000 K. The excitation temperature of all ions is 7000 K. The observed and synthetic spectra of both SN 1994D and SN 2003du have been flattened using the method of Jeffery et al. (2007).

The fits to the observed spectra in both of these figures are relatively good, and in both fits only permitted lines were considered. Even among the features which **SYNOW** cannot reproduce

accurately, most of the emission peaks and absorption troughs in the synthetic spectra form at the same wavelengths as in the observed spectra, and only the strengths of the features are disparate. (The exceptions to this are the wavelength range  $6600 - 7800 \text{ \AA}$  in SN 2003du and  $6600 - 7500 \text{ \AA}$  in SN 1994D, throughout which **SYNOW** fails completely to reproduce the observed features.) It would therefore be a remarkable coincidence if the observed features in these two objects arise from purely forbidden emission (Branch et al. 2005).

In addition to the circumstantial evidence for persistent resonance-scattering provided by these reasonably good **SYNOW** fits to several-months-old type Ia supernovae (SNe Ia), calculations by Hatano et al. (1999b) and Jerkstrand et al. (2011) further defend this claim. Hatano et al. (1999b) calculated the Sobolev optical depth (Equation 1 of that paper) for the most common ions observed in SN Ia optical spectra. In Figure 9c of that work they show the Sobolev LTE optical depth for Fe I & II and Co I & II for an iron-rich composition at 80 days post-explosion in a SN Ia model, and find that the optical depths for those ions can be as high as  $\tau \sim 50,000$ . Similarly, the simplified form of the Sobolev optical depth shown in Equation 39 of Jerkstrand et al. (2011) shows that the optical depths for some UV resonance lines (e.g., Mg II  $\lambda 2798$ ) can still be as high as  $\tau \sim 1000$  even eight *years* post-explosion.

In light of the evidence presented above for resonance-scattering at relatively late times in SNe Ia, we present a geometrical exploration of this phenomenon in the spirit of the Elementary Supernova approach of Jeffery & Branch (1990). Rather than attempt to discern exactly how late after a SN explosion resonance-scattering continues to contribute significantly to spectrum formation, we assume simply that the photosphere has receded and that the continuum opacity in the core of the SN is negligibly small. We replace the photosphere with a transparent core emitting non-blackbody continuum radiation and distribute ions both inside this “glowing” core and outside the core in a non-emitting shell. We then calculate emergent flux profiles for lines with parameterized optical depths in several different geometrical configurations. We scrutinize line formation and behavior in both isolated and blended cases. Because **SYNOW** inspired this model, the two naturally invite comparison, which we indulge throughout this work. In §2 we treat the case of pure continuum (no lines) in the core; in §3 we introduce a single line in the core; in §4 we surround the glowing core with a transparent, non-glowing shell and move the line to the shell; in §5 we account for the effects of multiple scattering by placing two lines in the core; §6 contains our discussion of the implications of our results on interpretation of late-time spectra of SNe; in §7 we conclude our work. Finally, we include Appendices which contain complete mathematical derivations so that all of our work may easily be reproduced.

## 2. A transparent, uniformly emitting core

We begin by assuming the SN is spherically symmetric. Under this circumstance it is natural to work in  $(p, z)$  coordinates, where  $p$  is the impact parameter of a ray relative to the center of the SN, such that the  $p = 0$  ray exactly bisects the SN; and  $z$  is orthogonal to  $p$ , with the  $z = 0$

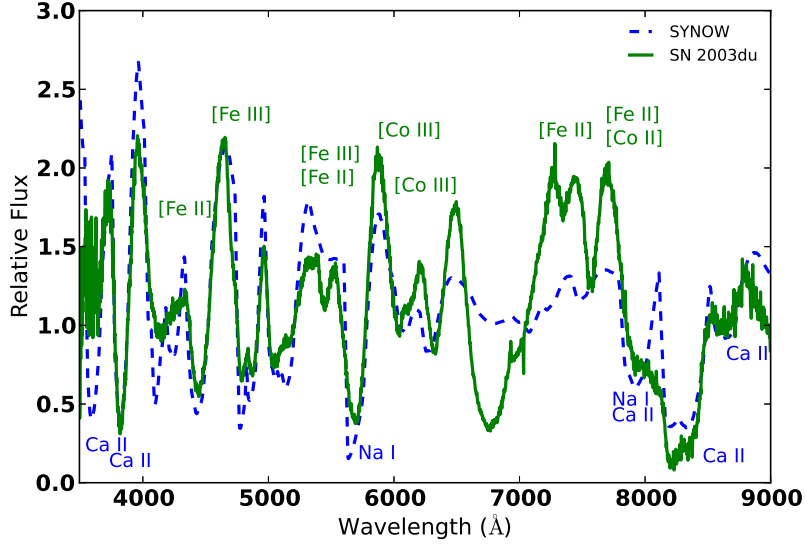


Fig. 1.— A SYNOW fit to the +87 day spectrum of SN 2003du. The synthetic spectrum contains Na I, Ca II, and Fe II, each with an excitation temperature of 7000 K. The photospheric velocity is  $7000 \text{ km s}^{-1}$ , and the spectrum has been divided through by the blackbody continuum. The permitted line identifications (in blue) are from the SYNOW fit, with Fe II features unlabeled. The alternative forbidden line IDs (in green) follow those in other SNe Ia made by Bowers et al. (1997).

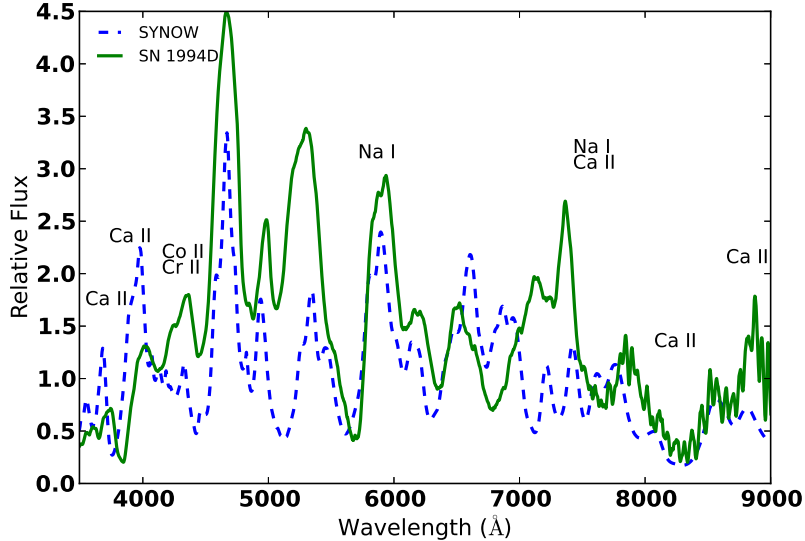


Fig. 2.— A SYNOW fit to the +115 day spectrum of SN 1994D. The synthetic spectrum contains Na I, Ca II, Cr II, Fe II, and Co II, each with an excitation temperature of 7000 K. The photospheric velocity is  $6000 \text{ km s}^{-1}$ , and the spectrum has been divided through by the blackbody continuum. As in Figure 1 the unlabeled features in the SYNOW spectrum are due to Fe II.

line also exactly bisecting the SN. We will at times transform to spherical polar coordinates for computational expedience, where the radial coordinate  $r$  satisfies

$$r^2 = p^2 + z^2. \quad (1)$$

We also assume that the SN undergoes homologous expansion,  $v = r/t$ , so that surfaces of constant line-of-sight velocity are vertical planes, that is, planes of constant  $z$ . We further assume that the observer is located at  $z \rightarrow -\infty$ , in which case all rays incident on the observer are parallel. Next, we assume that the photosphere has receded and has been replaced by a transparent, spherically symmetric core with outer radius  $r_c$  which emits continuum (but not blackbody) radiation. The post-photospheric spectra of many SNe Ia contain a flat and weak continuum which is either thermal in nature or, as Bowers et al. (1997) suggest, due to the sea of weak optical lines of lowly ionized Fe and Co. At very late times when the spectrum becomes truly nebular, there is no optical thermal continuum, but we do not seek to extend our methods into this very late regime. To mimic this pseudo-continuum we assign to the core a grey, spatially constant volume emissivity  $j_\lambda(r) = j$  for all radii  $r \leq r_c$  and all wavelengths  $\lambda$ . This assumption allows us to present simple analytic results; with only slight modification, our methods for calculating line profiles are amenable to chromatic emissivity.

## 2.1. Continuum only

In general, to calculate the emergent flux from a SN atmosphere one must first calculate the source function at all locations in the SN, followed by the emergent intensity of rays exiting the ejecta toward the observer. However, since in this model we neglect all continuum opacity, the source function is not a well defined quantity in the absence of lines. Therefore we write down immediately the emergent intensity of a constant  $p$  ray originating at the back<sup>1</sup> of the core and traversing toward the observer, without calculating the source function. When no lines are present the intensity of a ray passing through the core is proportional to its geometric length:

$$I(p) = 2j(r_c^2 - p^2)^{1/2}. \quad (2)$$

A representative intensity ray is shown in Figure 3. If instead the emissivity has spatial dependence,  $j = j(r)$ , the result has a more general form:

$$I(p) = \int_{-(r_c^2 - p^2)^{1/2}}^{(r_c^2 - p^2)^{1/2}} j((p^2 + z^2)^{1/2}) dz = 2 \int_0^{(r_c^2 - p^2)^{1/2}} j((p^2 + z^2)^{1/2}) dz \quad (3)$$

where we have transformed the argument of  $j$  since the intensity along a ray of constant  $p$  depends only on its  $z$  coordinate.

---

<sup>1</sup>In this discussion “front” and “back” refer to locations in the SN nearest to and farthest from the observer, respectively.

Already a physical peculiarity arises: limb darkening in the absence of scattering or absorption. The traditional interpretation of limb darkening in photospheric objects such as dwarf stars and young SNe is that intensity rays with large impact parameter  $p$ , that is, rays which emerge from the limb, reach an optical depth of  $\tau \simeq 1$  at shallower layers in the atmosphere than low-impact parameter rays. Under the assumption of local thermodynamic equilibrium (LTE), shallower locations in atmospheres have lower temperatures and thus weaker source functions, since LTE requires by definition that  $S = B$  where  $B$  is the Planck function. A weaker source function in turn leads to a lower intensity emergent ray, the cumulative result of which is limb darkening.

In the case of this post-photospheric model, however, high- $p$  rays accumulate less continuum as they proceed from the back of the object toward the observer. Such accumulation does not occur in photospheric-phase atmospheres of SNe except through lines in the atmosphere which scatter continuum photons from the blackbody photosphere into the ray; however, this contribution is small except when the line has an extraordinarily high optical depth.

Using Equation 2, the continuum flux at all wavelengths is given by

$$F_\lambda \equiv \int I_\lambda \cos \theta d\Omega = \frac{2\pi}{r_c^2} \int_0^{r_c} I_\lambda p dp = \frac{4\pi}{3} j r_c. \quad (4)$$

For clarity, and without loss of generality, hereafter we set  $j \equiv 1$ , so  $I_\lambda$ ,  $J_\lambda$ , and  $F_\lambda$  have units of length and the geometric nature of our results becomes apparent. In addition, since in homologous expansion  $v \propto r$ , we interchange lengths and velocities where convenient.

## 2.2. Mean intensity

We now calculate the mean intensity,  $J$ , both inside and outside the glowing core. Without any lines,  $J$  is not a particularly useful quantity in this model since we do not need it to calculate the emergent flux. However, when we add a single line to the core in §3 we require the source function to calculate the emergent intensity, and in the resonance-scattering approximation  $S = J$ .

By definition,

$$J_\lambda(r) \equiv \frac{1}{4\pi} \int I_\lambda(r) d\Omega = \frac{1}{2} \int_{-1}^1 I_\lambda(r) d\mu \quad (5)$$

where  $\mu \equiv \cos \theta$ , and we have applied to the radiation field the condition of azimuthal symmetry. Inside the core,  $r \leq r_c$ , so from Figure 4,

$$X = r\mu + (r^2\mu^2 + r_c^2 - r^2)^{1/2}. \quad (6)$$

Setting  $I_\lambda(r) = X(r)$ , plugging this into Equation 5, and using standard integral tables, we find

$$J(r) = \frac{1}{2r} \left\{ rr_c + \frac{(r_c^2 - r^2)}{2} \ln \left[ \frac{r_c + r}{r_c - r} \right] \right\}. \quad (7)$$

Calculating the mean intensity outside the core (with the line still inside the core) is slightly more complicated and we include the derivation in Appendix A. The result is:

$$J(r) = \frac{1}{2r} \left\{ rr_c + \frac{(r^2 - r_c^2)}{2} \ln \left[ \frac{r - r_c}{r + r_c} \right] \right\}. \quad (8)$$

Figure 5 shows the behavior of  $J(r)$  in units of  $r_c$  and for comparison the dilution factor  $W(r)$  (Mihalas 1978) is also shown. The shape of  $J$  is vary similar to that of a Gaussian and it is larger than  $W(r)$  until quite large  $r$ , where both functions behave as  $\frac{1}{4}(\frac{r_c}{r})^2$ . We emphasize that  $J$  peaks strongly at  $r = 0$ , a result which affects line formation significantly, as we will discuss in §3.

### 3. A line in the core

We now treat the case of a single line, forming inside the core. We assume, for simplicity, a constant Sobolev optical depth  $\tau$  in the line throughout the core. Before continuing, we note that the most profound effect of homologously expanding matter on the radiation field is that photons redshift with respect to the matter regardless of propagation direction. Therefore photons in a ray which starts at the back of the core and emerges toward the observer redshift continuously as they move along the ray. Referring to Figure 6, if a ray originates in front of the plane of constant  $z_{\text{res}}$  corresponding to the location in the core  $z = z_{\text{res}}$  where the line Doppler shifts into resonance with a particular wavelength point — that is, if  $p > (r_c^2 - z_{\text{res}}^2)^{1/2}$  — then the intensity of that ray is simply its continuum value, given by Equation 2. However, if the ray forms behind that plane — if  $p < (r_c^2 - z_{\text{res}}^2)^{1/2}$  — the line attenuates some of the continuum intensity by scattering photons out of the ray and therefore out of the observer’s line of sight. In the Sobolev approximation this attenuation manifests as a  $e^{-\tau}$  term multiplying the continuum intensity at the location of the line. In addition to attenuating the intensity along a ray, the line also contributes to the intensity via its source function  $S(r[z_{\text{res}}])$ . Specifically, the contribution is

$$I_{\text{line}} = S(1 - e^{-\tau}). \quad (9)$$

The two different types of rays are depicted in Figure 6. Their emergent intensities are

$$I_{z_{\text{res}}}(p) = \begin{cases} ((r_c^2 - p^2)^{1/2} - z_{\text{res}})e^{-\tau} + S(r)(1 - e^{-\tau}) + (r_c^2 - p^2)^{1/2} + z_{\text{res}} & p < (r_c^2 - z_{\text{res}}^2)^{1/2} \\ 2(r_c^2 - p^2)^{1/2} & p > (r_c^2 - z_{\text{res}}^2)^{1/2} \end{cases} \quad (10)$$

The integral over  $I_{z_{\text{res}}}(p)$  is straightforward except for the term containing the source function  $S(r)$ . To integrate this term we define

$$g(z_{\text{res}}) \equiv \int_0^{\sqrt{r_c^2 - z_{\text{res}}^2}} S(r) p dp = \int_0^{\sqrt{r_c^2 - z_{\text{res}}^2}} \frac{1}{2r} \left[ rr_c + \frac{r_c^2 - r^2}{2} \ln \left[ \frac{r_c + r}{r_c - r} \right] \right] p dp. \quad (11)$$

We then transform the integration variable from  $p$  to  $r$ , which leads to

$$g(z_{\text{res}}) = \int_{z_{\text{res}}}^{r_c} \frac{1}{2r} \left[ rr_c + \frac{r_c^2 - r^2}{2} \ln \left[ \frac{r_c + r}{r_c - r} \right] \right] r dr.$$

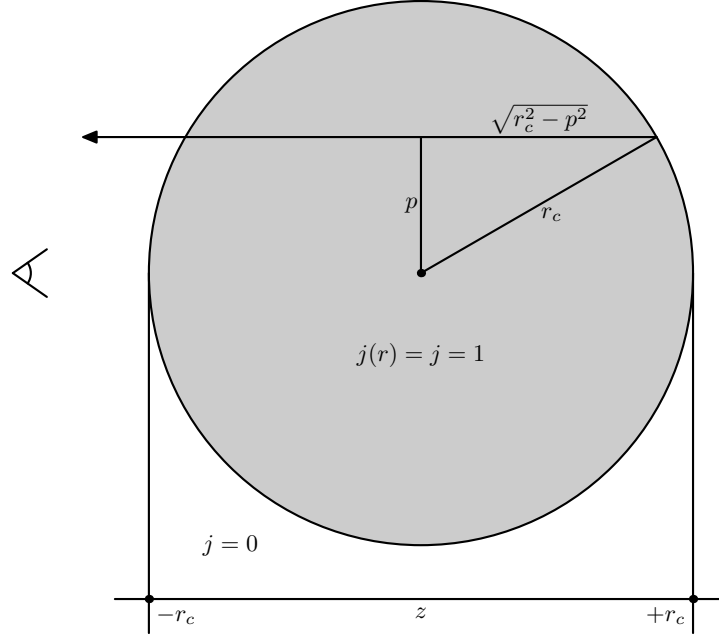


Fig. 3.— A continuum ray in the core of the SN. In this figure and all which follow, we use grey shading to label the continuum-emitting region.

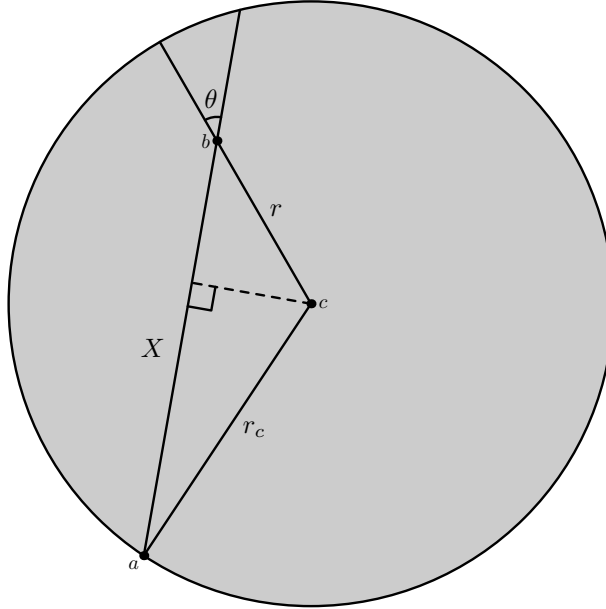


Fig. 4.— Geometric configuration used to calculate  $J(r \leq r_c)$  both for pure continuum and for a single line in the core.  $X$  is the magnitude of the vector  $\vec{ab}$ ,  $r_c$  is that of  $\vec{ac}$ , and  $r$  is that of  $\vec{bc}$ .



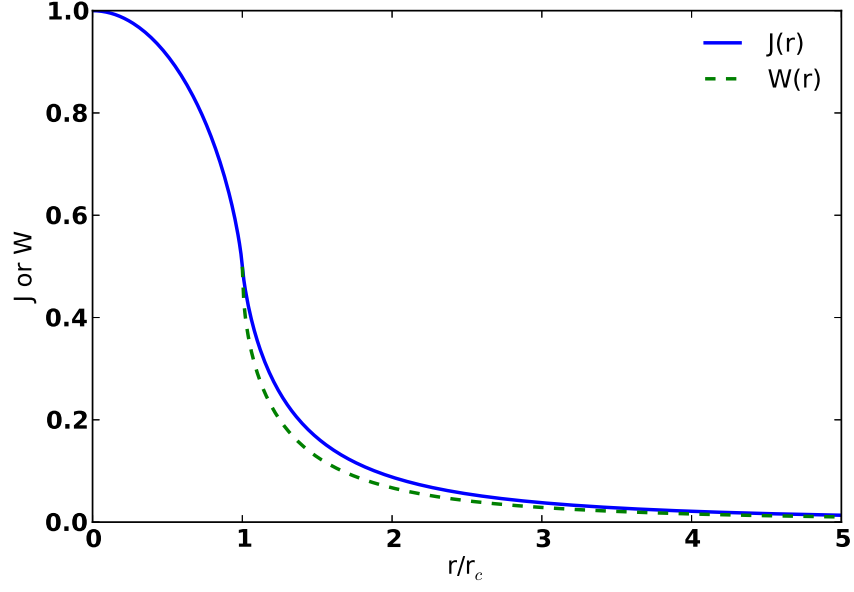


Fig. 5.— The profile of  $J(r)$  and  $W(r)$ , where  $W$  is the dilution factor.

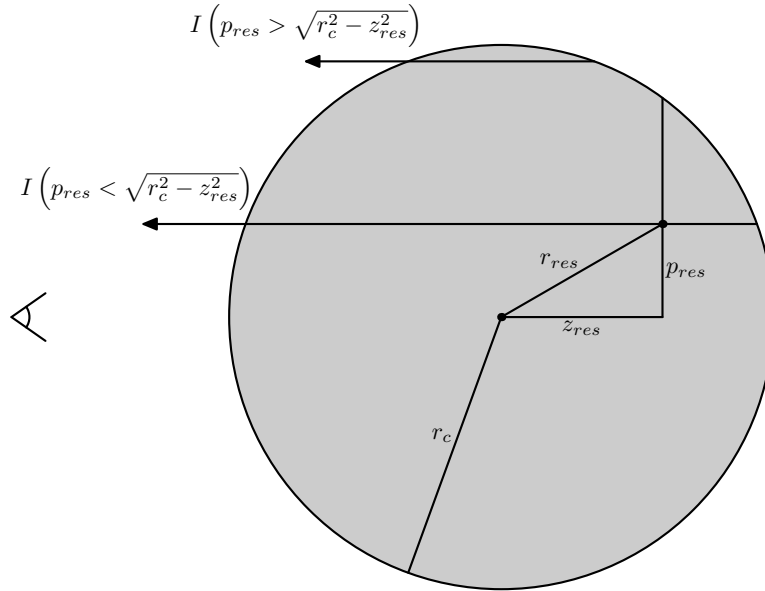


Fig. 6.— Intensity rays with a single line in the core.

This integral is still unwieldy, so we transform integration variables once again by defining

$$\mu \equiv \frac{z_{\text{res}}}{r}$$

and

$$\mu_{\text{res}} \equiv \frac{z_{\text{res}}}{r_c}$$

from which we find

$$\frac{r}{r_c} = \frac{\mu_{\text{res}}}{\mu}.$$

We then change the integration variable from  $r$  to  $\mu$ , which yields

$$g(z_{\text{res}}) = \frac{r_c^3}{2} \mu_{\text{res}}^2 \int_{\mu_{\text{res}}}^1 \left[ 1 + \frac{\mu^2 - \mu_{\text{res}}^2}{2\mu\mu_{\text{res}}} \ln \left[ \frac{1 + \mu_{\text{res}}}{1 - \mu_{\text{res}}} \right] \right] \frac{d\mu}{\mu^3}.$$

The result is

$$g(z_{\text{res}}) = \frac{r_c^3}{6} \left[ 1 + 2 \ln 2 - \mu_{\text{res}}^2 - \frac{\mu_{\text{res}}}{2} (3 - \mu_{\text{res}}^2) \ln \left[ \frac{1 + \mu_{\text{res}}}{1 - \mu_{\text{res}}} \right] - \ln(1 - \mu_{\text{res}}^2) \right]. \quad (12)$$

The remainder of Equation 4 poses little challenge and leads directly to an analytic result for the flux profile for the constant- $\tau$  case:

$$F(z_{\text{res}}) = \frac{2\pi}{r_c^2} \left[ \frac{2r_c^3}{3} + (1 - e^{-\tau}) \left[ g(z_{\text{res}}) + \frac{z_{\text{res}}(r_c^2 - z_{\text{res}}^2)}{2} - \frac{r_c^3 - |z_{\text{res}}|^3}{3} \right] \right]. \quad (13)$$

We remark here that, although Equation 4 defines the flux as a function of wavelength, we have derived Equation 13 in terms of the coordinate  $z_{\text{res}}$ . One transforms between  $z \leftrightarrow \lambda$  using the first-order Doppler formula,

$$z = r_{\text{max}} \left( \frac{c}{v_{\text{max}}} \right) \frac{\lambda - \lambda_0}{\lambda_0}, \quad (14)$$

where  $r_{\text{max}}$  ( $v_{\text{max}}$ ) is the maximum radius (velocity) of the ejecta. We show in Figure 7 the line profiles of Na I D,  $\lambda 5892$ , with several different optical depths.<sup>2</sup> For comparison we show in Figure 8 the profile of Na I D as calculated by **SYNOW**, with the same optical depths as in Figure 7.

The profiles in both plots appear quite P Cygni-like, but differences do exist between them. We highlight two in particular. First, when a photosphere is present as in **SYNOW**, the emission peak of a line profile is located at its rest wavelength, regardless of the velocity of the material forming the line in the SN atmosphere. This fact simplifies enormously the task of identifying isolated lines in a SN spectrum (Jeffery & Branch 1990). In the post-photospheric model, however, the emission peak is *not* centered on the line rest wavelength; rather it is considerably redshifted. As Figure 7 shows, with a core outer edge velocity of only 3000 km s<sup>-1</sup>, the emission peak is  $\sim 15$  Å redward of

---

<sup>2</sup>Examining Figures 1 and 2, identification of Na I is ubiquitous; we therefore use the Na I D line for illustrative purposes.

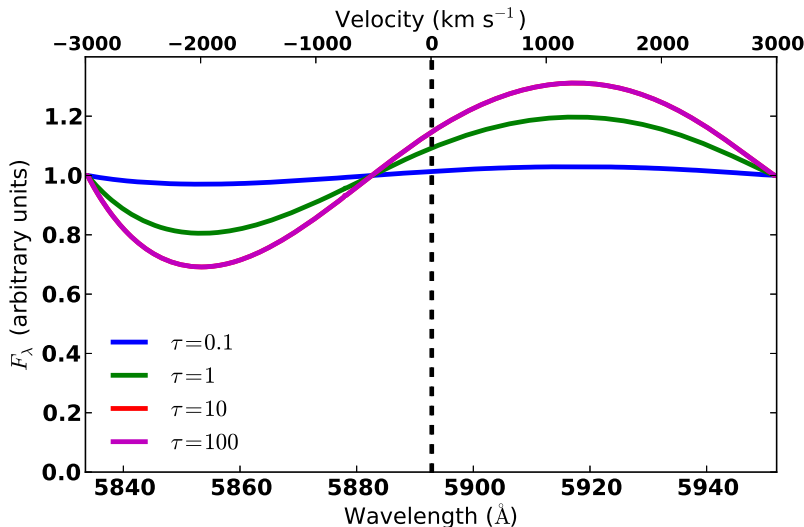


Fig. 7.— Flux profiles for Na I D,  $\lambda 5892$ , in the post-photospheric model, with spatially constant optical depth and an outer core velocity of  $3000 \text{ km s}^{-1}$ . The vertical dashed line indicates the rest wavelength of the line. The  $\tau = 10$  and  $\tau = 100$  profiles overlap almost exactly and are indistinguishable in this figure. In contrast to SYNOW the red emission peak does not occur at the rest wavelength, but rather is redshifted by an amount independent of optical depth.

the line rest wavelength. Though the absorption component of a P Cygni profile is used more often than the corresponding emission to identify lines in a spectrum (since the former dominates the latter in overlapping lines; see Jeffery & Branch 1990), this redshift could lead to misidentification of lines in intermediate- or late-time SN spectra.

What is the origin of the emission peak redshift? This question is easier to answer in the limit  $\tau \rightarrow \infty$ , the line profile for which would look identical to that of  $\tau = 100$  in Figure 7. In the  $\tau \rightarrow \infty$  case the line at the resonance point  $z_{\text{res}}$  scatters *all* continuum photons forming in the ray segment  $z > z_{\text{res}}$  out of the ray, and the contribution of the line to the intensity along that ray is simply  $I_{\text{line}} = S(r[z_{\text{res}}])$ . Thus only two sources of emission contribute to the flux at a given wavelength: 1.) the continuum emission in front of the resonance plane at  $z = z_{\text{res}}$ ; and 2.) the source function at the plane. If the plane is located near the back of the core,  $z \lesssim r_c$ , the portion of the core’s volume which emits continuum photons which escape unscattered and reach the observer is large. However, because the surface area of the plane is small when  $z$  is close to  $r_c$ , and because from Figure 5 we see that  $S$  is small at  $r \sim r_c$  — only half of its maximum value — the emission contribution from the source function on the plane is in turn relatively small.

As the resonance plane moves forward (to bluer wavelengths, smaller  $z$ ), the volume of the emitting core in front of the plane decreases, but the surface area of the plane grows, and Figure 5 shows that the source function at the plane grows quickly as well. From  $\frac{1}{3}r_c \lesssim z \lesssim r_c$  the scattering

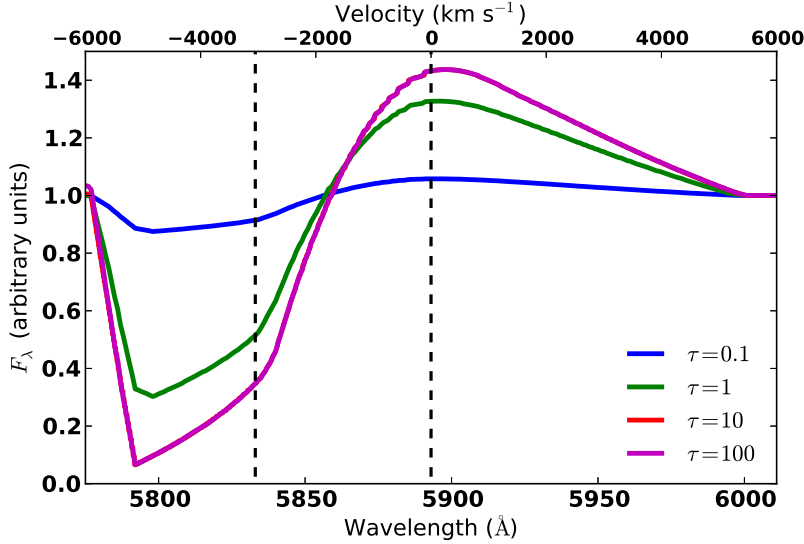


Fig. 8.— Flux profiles for Na I D in SYNOW, with photospheric velocity  $3000 \text{ km s}^{-1}$  and spatially constant optical depth. The maximum velocity of the line-forming region is  $6000 \text{ km s}^{-1}$ . The right dashed vertical line indicates the rest wavelength of the Na I D line ( $\lambda 5892$ ), and the left vertical line indicates the blueshifted rest wavelength of Na I D at the photospheric velocity. The  $\tau = 10$  and  $\tau = 100$  profiles overlap almost exactly and are indistinguishable in this figure. Unlike the profiles in Figure 7, the emission peak in the SYNOW case remains fixed at the line rest wavelength regardless of the optical depth.

emission from the resonance plane more than compensates for the diminishing continuum emission from the core, causing the flux to increase monotonically as one moves blueward in that region, eventually reaching the emission peak, which in Figure 7 is  $\sim 5915 \text{ \AA}$ . Blueward of this peak, despite the fact that  $S$  increases monotonically until reaching  $z = 0$ , the surface area of the plane increases only slightly when  $z \gtrsim 0$  and the now very large resonance plane occults so much of the core over a small shift  $\Delta z$  that it can no longer compensate for the large amount of emission removed from the volume of the core behind it, causing the flux to decrease as  $z$  becomes smaller. This transition point exists *redward* of  $z = 0$  and thus the emission peak of the P Cygni profile is redder than the rest wavelength of the line.

Blueward of  $z = 0$ , that is,  $-r_c < z < 0$ , the area of the resonance plane begins to decrease, now only obscuring a cylindrical volume of the glowing core. Even though the length of this occulted cylinder increases as  $z$  becomes more negative, its radius decreases, and the portion of the total volume of the core that this cylinder comprises decreases as well. The now-unocculted limbs of the core, emitting continuum which the resonance plane can no longer scatter away, grow in volume and eventually compensate once again for the cylindrical volume obscured by the plane, causing the flux to increase. This transition point manifests as the absorption minimum in the flux profile

( $\sim 5855 \text{ \AA}$  in Figure 7), blueward of which the flux increases until the resonance plane reaches  $z = -r_c$  and we recover pure continuum.

The second difference between the line profiles with and without a photosphere is that, in the former, the flux in strong lines deviates from the continuum by a large amount, whereas in the latter the changes are small. The flux in the absorption minimum of the  $\tau_0 = 100$  line in Figure 8, for example, is 80% lower than the continuum value. In our post-photospheric model, on the other hand, even the strongest line in Figure 7 departs by only up to 30% from the continuum. That the post-photospheric model exhibits such small departures from continuum is due to the ability of a small portion of the core to emit unscattered photons toward the observer even when the resonance plane is near the front. In the **SYNOW** case, the shell above the photosphere does not emit any continuum, so when the plane is close to the front of the ejecta, only scattering from the plane itself contributes to the flux, causing it to be extremely low at the absorption minimum.

The physical simplicity of constant  $\tau$  line profiles such as those in Figures 7 and 8 readily facilitates analysis of line formation in SN ejecta, as we have just seen. However, one must also be aware of complicating effects such as the inhomogeneous structure of SNe, viz. the velocity-dependent density profile. In the Elementary Supernova framework one assumes implicitly that  $\tau = \tau(\rho)$ , where  $\rho$  is the matter density, and accounts for this by writing  $\tau$  as, e.g., an exponential or power law function which decreases with increasing velocity. To illustrate how a variable optical depth affects line formation we show in Figure 9 the line profile of Na I D in our post-photospheric model with  $\tau(v) = \tau_0 \exp(-v/v_e)$ , where  $\tau_0$  is a constant and  $v_e = 500 \text{ km s}^{-1}$ . Again, for comparison, we show in Figure 10 a **SYNOW** plot of the same line with the same exponential  $\tau$  profile.

In the post-photospheric case, shown in Figure 9, the relationship between velocities and the positions of the emission maximum and absorption minimum is not immediately obvious. Like the **SYNOW** line profiles, shown in Figure 10, the blue edge of the absorption component (not of the absorption *minimum*; see  $5835 \text{ \AA}$  in Figure 9, and  $5775 \text{ \AA}$  in Figure 10) indicates the maximum velocity of the line-forming material, although in blended cases this can be difficult to discern. Unlike **SYNOW**, in this model both the peak and trough continuously redshift and blueshift, respectively, as the line optical depth increases. In the **SYNOW** case, on the other hand, the separation between the rest wavelength of the line and the minimum of the blueshifted absorption component indicates the velocity of the photosphere and thus the minimum velocity of the line-forming material itself (assuming the material is not “detached” above the photosphere, Jeffery & Branch 1990). Only when the line optical depth is extremely high does the location of the absorption minimum begin to move blueward of the photospheric blueshift, as in the  $\tau_0 = 100$  line in Figure 10. For each of the three weaker lines in that figure, one can simply measure the blue edge of the absorption minimum,  $\sim 5830 \text{ \AA}$ , then calculate the photospheric velocity,  $\sim 3000 \text{ km s}^{-1}$ .

We also note that the  $\tau = 10$  and  $\tau = 100$  line profiles in Figures 7 and 8 appear identical, whereas in Figures 9 and 10 the  $\tau_0 = 10$  and  $\tau_0 = 100$  profiles are distinct. This difference is due to

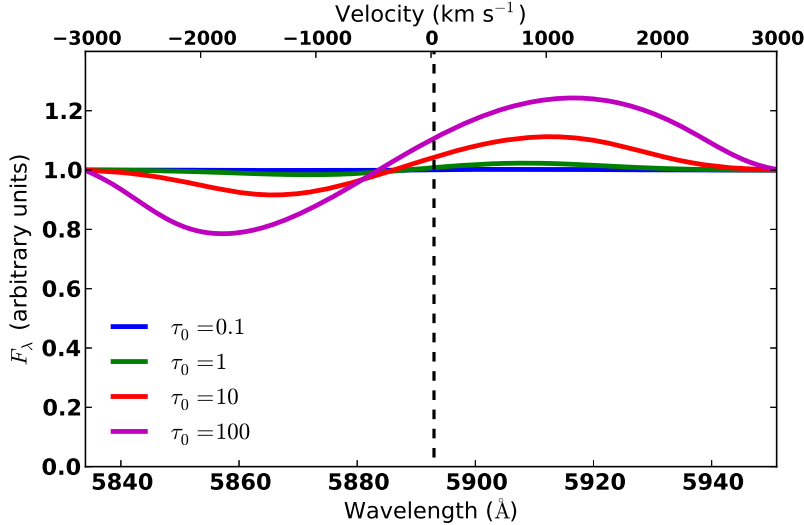


Fig. 9.— Flux profiles for Na I D,  $\lambda 5892$ , in the post-photospheric model with outer edge core velocity  $3000 \text{ km s}^{-1}$  and a line optical depth following an exponential decay,  $\tau(v) = \tau_0 \exp(-v/v_e)$ , where  $v_e = 500 \text{ km s}^{-1}$ . The vertical dashed line indicates the rest wavelength of the line. In contrast to **SYNOW**, the red emission peak does not occur at the rest wavelength, but is rather significantly redshifted by an amount which depends on the strength of the line. Also unlike **SYNOW**, the blue absorption minimum blueshifts continuously with increasing optical depth.

the velocity dependence of  $\tau$ : in the former pair of figures, the optical depth is constant everywhere, leading to a saturated profile throughout the line-forming region when  $\tau \geq 10$ . In the latter pair, on the other hand,  $\tau$  decreases exponentially with increasing velocity, so the line samples such large optical depths at only very low velocities. This velocity dependence affects line formation outside the core in exactly the same way (cf. §4).

#### 4. A line outside the core

Having explored in detail the geometric effects of continuum emission on line formation in the core, we now introduce a non-emitting, transparent shell around the core, with outer radius  $r_s$ , where  $r_s > r_c$ . In this region there is no continuum emission and line formation occurs in exactly the same way as in **SYNOW**. Therefore, unlike the case discussed in §3, the line forming region now exists *outside* the core, rather than inside. We include the shell in this model to account for the possibility of intermediate mass elements such as Ca II forming lines at late times above the material which has been burned all the way to the iron-peak.

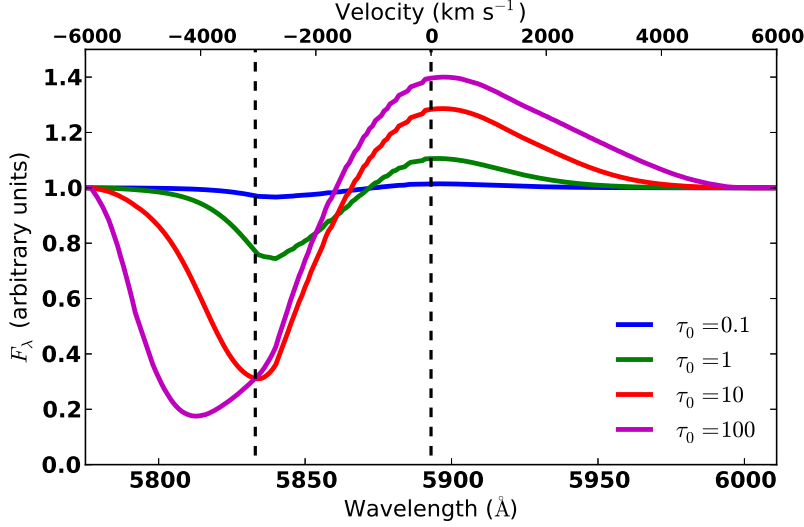


Fig. 10.— Flux profiles for Na I D,  $\lambda 5892$ , in SYNOW, with photospheric velocity  $3000 \text{ km s}^{-1}$  and a line optical depth following an exponential decay,  $\tau(v) = \tau_0 \exp(-v/v_e)$ , where  $v_e = 500 \text{ km s}^{-1}$ . The maximum velocity of the line-forming region is  $6000 \text{ km s}^{-1}$ . The right vertical dashed line indicates the rest wavelength of the line, and the left dashed line indicates the wavelength of Na I D blueshifted to the photospheric velocity. Except for extremely high optical depths, the blue edge of the absorption minimum remains fixed at the photospheric velocity; and for all optical depths, the red emission peak remains at the rest wavelength of the line.

#### 4.1. Intensity for a line outside the core

We must now consider a number of possible ways that the line and a particular ray can interact. First, if the ray has impact parameter  $p > r_c$  then it never intersects the core and, regardless of the location of the line resonance point  $z_{\text{res}}$ , the ray's emergent intensity is

$$I_{z_{\text{res}}}(p) = S(r[z_{\text{res}}])(1 - e^{-\tau}) \quad (15)$$

where  $S(r)$  is now the source function *outside* the core, given by Equation 8, and

$$\tau = \tau(r[z_{\text{res}}]). \quad (16)$$

If the line has  $p < r_c$  but  $z_{\text{res}} < -\sqrt{r_c^2 - p_{\text{res}}^2}$ , then the line attenuates the continuum ray from the core:

$$I_{z_{\text{res}}}(p) = S(r[z_{\text{res}}])(1 - e^{-\tau}) + 2(r_c^2 - p^2)^{1/2} e^{-\tau}. \quad (17)$$

Finally, if the line has  $p < r_c$  and  $z_{\text{res}} > \sqrt{r_c^2 - p_{\text{res}}^2}$ , then it does *not* attenuate the core continuum and the emergent intensity is

$$I_{z_{\text{res}}}(p) = S(r[z_{\text{res}}])(1 - e^{-\tau}) + 2(r_c^2 - p^2)^{1/2}. \quad (18)$$

These three cases are shown in Figure 11.

#### 4.2. Flux for a line outside the core

While  $F_\lambda$  proceeds simply from  $I_\lambda$  in the case  $r \leq r_c$ , its form is much more complicated in the  $r > r_c$  regime. In particular the flux integral takes a unique form in five different regions. We show the five zones in Figure 12.

1.  $-r_s < z < -(r_s^2 - r_c^2)^{1/2}$

$$\begin{aligned} F_z = & \frac{4\pi}{r_c^2} e^{-\tau} \int_0^{(r_s^2 - z^2)^{1/2}} (r_c^2 - p^2)^{1/2} p dp \\ & + \frac{4\pi}{r_c^2} \int_{(r_s^2 - z^2)^{1/2}}^{r_c} (r_c^2 - p^2)^{1/2} p dp \\ & + \frac{2\pi}{r_c^2} (1 - e^{-\tau}) \int_0^{(r_s^2 - z^2)^{1/2}} S(r[p]) p dp \end{aligned}$$

2.  $-(r_s^2 - r_c^2)^{1/2} < z < -r_c$

$$F_z = \frac{4\pi}{3} r_c e^{-\tau} + \frac{2\pi}{r_c^2} (1 - e^{-\tau}) \int_0^{(r_s^2 - z^2)^{1/2}} S(r[p]) p dp$$

3.  $-r_c < z < 0$

$$\begin{aligned} F_z = & \frac{4\pi}{r_c^2} \int_0^{(r_c^2 - z^2)^{1/2}} (r_c^2 - p^2)^{1/2} p dp \\ & + \frac{4\pi}{r_c^2} e^{-\tau} \int_{(r_c^2 - z^2)^{1/2}}^{r_c} (r_c^2 - p^2)^{1/2} p dp \\ & + \frac{2\pi}{r_c^2} (1 - e^{-\tau}) \int_{(r_c^2 - z^2)^{1/2}}^{(r_s^2 - z^2)^{1/2}} S(r[p]) p dp \end{aligned}$$

4.  $0 < z < r_c$

$$F_z = \frac{4\pi}{3} r_c + \frac{2\pi}{r_c^2} (1 - e^{-\tau}) \int_{(r_c^2 - z^2)^{1/2}}^{(r_s^2 - z^2)^{1/2}} S(r[p]) p dp$$

5.  $r_c < z < r_s$

$$F_z = \frac{4\pi}{3} r_c + \frac{2\pi}{r_c^2} (1 - e^{-\tau}) \int_0^{(r_s^2 - z^2)^{1/2}} S(r[p]) p dp$$

Figure 13 depicts single-line profiles with different values of  $\tau$ . We first note the resemblance of these line profiles to those of SYNOW shown in Figure 8. This is not surprising, given that the only



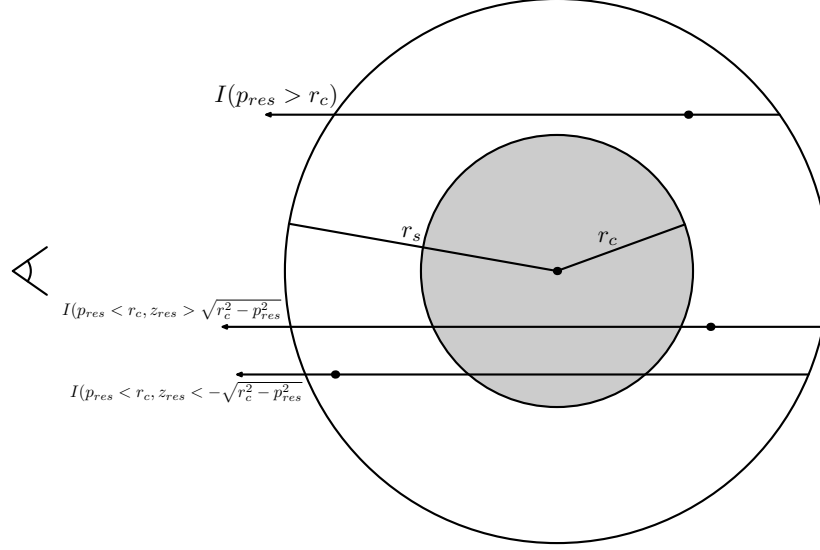


Fig. 11.— The three types of intensity rays for the core+shell configuration.

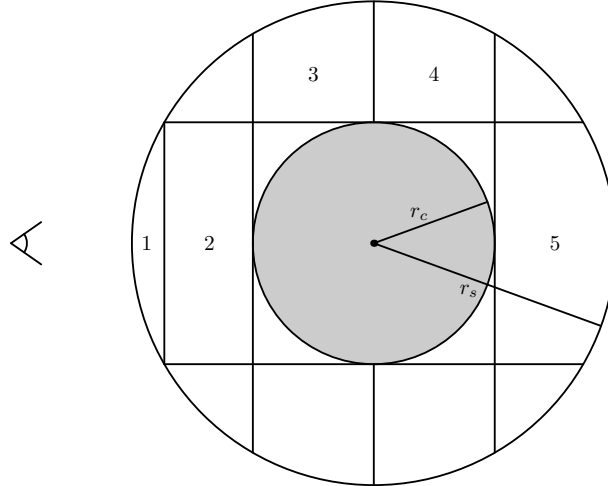


Fig. 12.— The five flux regions in the core+shell configuration.

difference between the two models is that in **SYNOW** the core is opaque while in the post-photospheric model it is transparent. Both exhibit strong deviations from the continuum flux value, especially in the absorption component. We discussed in §3 the cause of this near-zero flux in the absorption component of the line.

There is one major difference between the line profiles in Figures 8 and 13: the flat-topped emission component in the latter. To discern the source of this plateau in the spectrum, we conduct a geometric analysis similar to that presented in §3, again studying the limit  $\tau \rightarrow \infty$ . Starting with the resonance plane at the back of the shell,  $z = r_s$ , we see that as it moves forward toward the observer, its surface area grows, which leads to the flux increase from 6010 Å blueward to 5950 Å in Figure 13.

When the resonance plane reaches the back edge of the core and begins to move forward through it, that is, when  $0 < z_{\text{res}} < r_c$ , the core projects onto the plane a central circular region where  $\tau = 0$  and continuum emission from the core is unattenuated. The component of the plane which samples the optical depth in the shell is a ring with area

$$A = \pi(r_s^2 - z_{\text{res}}^2) - \pi(r_c^2 - z_{\text{res}}^2) = \pi(r_s^2 - r_c^2). \quad (19)$$

From this equation we see that  $A$  is constant when  $0 < z_{\text{res}} < r_c$ ; this constancy is the cause of the emission plateau in Figure 13.

When  $-r_c < z_{\text{res}} < 0$ , the plane begins to obscure the core, starting at the core’s limb, and scatters an increasing amount of the continuum emission out of the observer’s line of sight. When  $z_{\text{res}} < -r_c$  the entire core is obscured and the only emission from the ejecta comes from the source function at  $z_{\text{res}}$ . In the region  $-r_s < z_{\text{res}} < -r_c$ , line formation occurs in exactly the same way as in **SYNOW**, leading to the absorption trough in Figure 13 which is almost identical to that of the **SYNOW** profile shown in Fig. 8.

The constant-flux emission in the spectra in Figure 13 is the most distinguishing feature of our post-photospheric model. In §6 we will consider a nebular line-forming region with a “hole” devoid of line optical depth, and there we will encounter a geometric conspiracy similar to the one presented in this section, leading to similarly flat features in line profiles. We remark in addition that **SYNOW** can produce flat-topped emission features in a spectrum by detaching lines from the photosphere. Thus we conclude that in general a plateau-shaped line emission feature indicates some kind of missing line opacity.

## 5. Two lines in the core

We now study the case of two resonance lines in the core. Understanding the ways in which multiple lines “interact” via their overlapping flux profiles, and in turn being able to identify them individually, is critical to interpreting observed spectra since, in all epochs of a SN, its optical spectrum exhibits severe line blending.

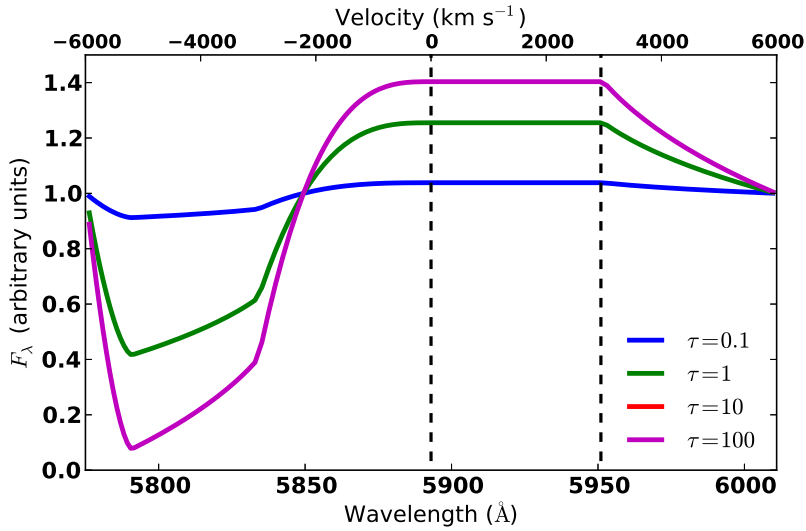


Fig. 13.— Flux for Na I D in the shell, with core velocity  $3000 \text{ km s}^{-1}$  and outer edge shell velocity  $6000 \text{ km s}^{-1}$ . The rest wavelength of the line is  $\lambda_0 = 5892 \text{ \AA}$ , indicated by the left vertical dashed line. The right dashed line indicates the rest wavelength of Na I D redshifted to the back edge of the core, at which point the emission peak forms a plateau. For  $r_c \leq r \leq r_s$ ,  $\tau = \text{constant}$  and for  $r \leq r_c$ ,  $\tau = 0$ . The  $\tau = 10$  and  $\tau = 100$  profiles overlap almost exactly and are indistinguishable in this figure.

In the resonance-scattering approximation, for any number of lines in the core, the source function of the bluest line always has the single-line form given in Equation 7, since there are no bluer photons in the radiation field which can redshift into resonance with it. The second bluest line then interacts only with its bluer neighbor; the third bluest line interacts with its two bluer neighbors; etc. In computational terms this means that one calculates the source function for each line starting with the bluest and moving redward. The details of the calculation are shown in Appendix B.

We first consider the case  $v_{\text{core}} = 3000 \text{ km s}^{-1}$ , and we hold the optical depths of both lines fixed everywhere in the core,  $\tau_B = \tau_R = 1$ . We then set the rest wavelength of the blue line to  $2850 \text{ \AA}$  and decrement the rest wavelength of the red line from  $3000 \text{ \AA}$ , where the lines are too far apart in wavelength space to blend in the spectrum, to  $2855 \text{ \AA}$ , where the lines overlap completely. The result is shown in Figure 14. In this figure we find that line blending in the post-photospheric case occurs in essentially the same way as in the SYNOW case (Jeffery & Branch 1990). Specifically, the absorption component of the red line completely overwhelms the emission of the blue line, and also, when the two lines overlap perfectly (the bottom-right panel of Figure 14), the redshifted emission component appears the same as the single-line case, but the absorption is much deeper.

One peculiar feature of Figure 14 is that, when the lines overlap only partially, the emission component of the blue line acquires a triangular shape. In fact, in the upper-right panel of that figure, the triangular emission peak is nearly symmetrical. However the abrupt (perhaps unrealistic) drop in  $\tau$  at the edge of the core in this calculation may somewhat exaggerate this triangular feature.

In this section we have restricted our discussion to the interaction between two lines confined to the core. However, with the introduction of multiple lines, many other types of interactions are possible. As an example, in Appendix B.2 we construct the geometric framework for the two-line case where both lines are outside the core. However the situation is more complex due to the myriad combinations of line locations as well as their combined interaction with the core and shell. We thus defer a thorough examination of all the possible effects that can occur in this case, including the effects of the photosphere before it has receded completely, to a future work (B. Friesen & R. C. Thomas, in preparation).

## 6. Discussion

Much recent work analyzing SNe Ia spectra has focused on the importance of asymmetries (Maeda et al. 2010, 2011; Maund et al. 2010; Foley & Kasen 2011; Foley et al. 2012). However, the spectra produced by this model illustrate a potentially significant complication in interpreting spectra at late times in SNe Ia, specifically in the interpretation of line emission in the absence of scattering. To illustrate this point we refer to the work of Maeda et al. (2010, 2011), who interpret observed blueshifts and redshifts of Fe lines in nebular spectra as resulting from asymmetric clumps of iron-peak material moving toward and away from the observer, respectively, in the optically thin

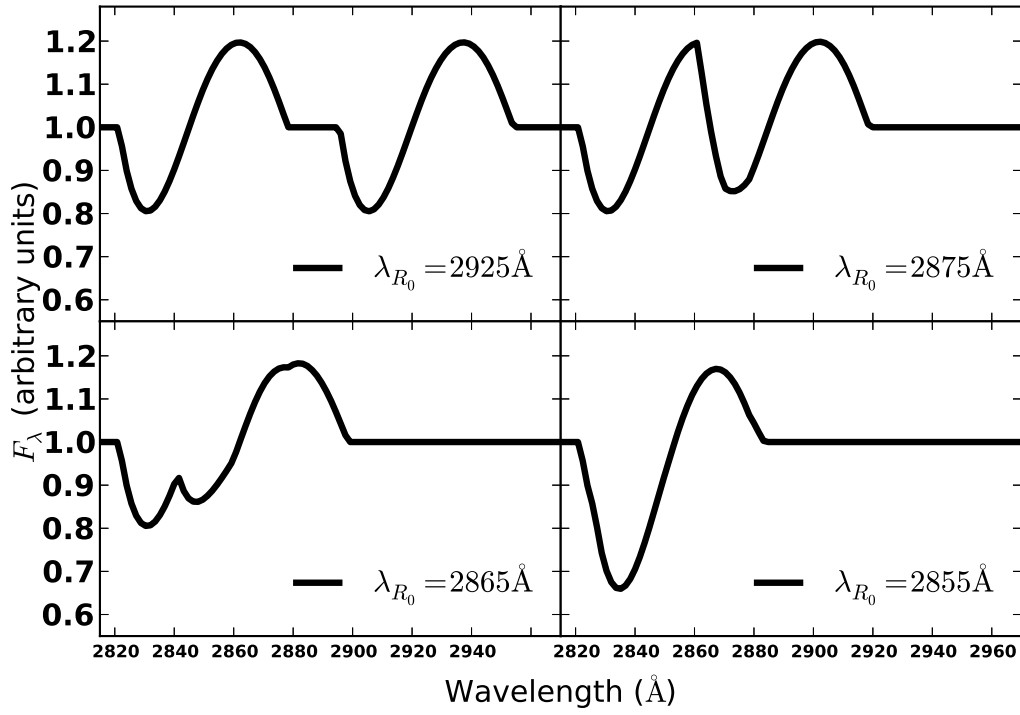


Fig. 14.— Interaction of two lines in the core as they blend together due to Doppler broadening. The rest wavelength of the blue line is fixed at  $\lambda_{B_0} = 2850 \text{\AA}$ , while the rest wavelength of the red line moves blueward. The optical depths of both lines are fixed at  $\tau_B = \tau_R = 1$ .

SN Ia ejecta. This interpretation implies that the explosion of a white dwarf resulting in a SN Ia is itself highly asymmetric, but relies heavily upon the assumption that spectral features at late times arise *only* through forbidden transitions of atomic lines due to the low gas density, and that the resulting emission profiles are distributed roughly symmetrically about the rest wavelength. Indeed, this assumption has become widespread in nebular spectrum synthesis since the pioneering work of Axelrod (1980). However, if an appreciable amount of resonance-scattering is present at this epoch, our results show that in the presence of significant continuum emission, a perfectly spherically symmetric distribution of matter produces a redshifted emission component. It remains unclear what effect, if any, that resonance-scattering has on the sample considered in Maeda et al. (2010) since the objects in their study were often several hundred days older than the objects we attempted to fit using SYNOW in Figures 1 and 2.

Maund et al. (2010) studied polarization measurements of the objects in Maeda et al. (2010) for which such data were available, and drew similar conclusions as Maeda et al. (2010), that is, that asymmetry alone may explain the diversity observed in SNe Ia. The survey in Maund et al. (2010) was biased in that polarization data existed only for SNe with redshifted emission peaks for particular lines of Fe II and Ni II, but nevertheless we note that, at intermediate times, for many features there are multiple possible line identifications, and redshifted emission can result from either optically thin, receding ejecta, or, as shown in Figure 7, from spherically symmetric ejecta with large line optical depth. While the very late data (Maeda et al. 2010; Maund et al. 2010) may indeed be showing the inferred asymmetry, our results show that one should indeed be cautious about the epoch of the data when interpreting redshifted emission profiles.

Finally, we consider another significant effect of resonance-scattering at late times in SNe. Studies of late-time line profiles and the imaging of the supernova remnant S Andromeda (Höflich et al. 2004; Motohara et al. 2006; Fesen et al. 2007; Gerardy et al. 2007; Maeda et al. 2010) have lead to the suggestion that a “nickel hole” exists in at least some SNe Ia. In optically thin media, a central region devoid of line-forming material manifests in a spectrum as a flat-topped emission feature in the spectrum; Höflich et al. (2004) find just this when studying the [Fe II]  $\lambda 16,440$  line in a spectrum of SN 2003du taken  $\sim 300$  days after explosion, suggesting that  $^{56}\text{Fe}$  and therefore  $^{56}\text{Ni}$  were absent in the central part of the SN ejecta. However, the IR observations in these studies are quite noisy, and if the same effect could be observed earlier, or in stronger lines, there would be more flux, allowing statistics to be built up on the existence of a nickel hole in SNe Ia, which would provide important constraints on the underlying explosion model.

With this in mind we explore the possibility that one may observe a similar plateau feature inside the glowing core by carving out regions of zero optical depth in a resonance-scattering line. To study this, we return to the core-only model, with velocity  $3000 \text{ km s}^{-1}$ , and set the rest wavelength of a single line in the core to  $3000 \text{ \AA}$ . We then set the optical depth of the line to  $\tau = 1$ , and proceed to exclude this optical depth from progressively larger portions of the core’s central region. The resulting line profiles are shown in Figure 15. The classical rounded profile is replaced by a flat profile, but there still exists both an emission peak and an absorption trough. This result

corroborates the plateau effects we studied in §4 — Figure 13 already showed that when a region of large line optical depth surrounds a region of zero optical depth, flat-topped components can appear in the spectral line profiles.

## 7. Conclusions

We have presented the geometric framework for a post-photospheric model of a SN, making simple assumptions about its emissivity and source function, in an attempt to explore the effects of resonance-scattering in optically thick lines in SN atmospheres in epochs where such scattering processes are rarely considered. Our model is inspired by and similar to the Elementary Supernova model, but the substitution of a photosphere for a transparent but continuum-emitting core leads to significant differences in line formation. The most noticeable difference is that the emission peak of a line is redshifted from its rest wavelength, even though the model is spherically symmetric. This property may affect the interpretation of SN spectra in post-photospheric phases, when asymmetric effects on line formation become influential.

Our model remains mostly within the geometric confines of the Elementary Supernova model, and choices about its properties different than the ones made here are possible. For example, one may assume that severe line blending in the core creates a pseudo-continuum, leading to a source function in the shell exactly equal to that assumed in SYNOW:

$$S = W(r)J,$$

where  $W(r)$  is the dilution factor. We have also chosen to parameterize all line optical depths rather than calculating them in any self-consistent manner, e.g., by solving rate equations. We believe our choices in these matters have resulted in a level of detail commensurate with the simplicity of this model.

To explore fully the other implications of resonance-scattering on line formation at post-photospheric times in SNe Ia we are currently incorporating the formalism presented in this work into SYNAPPS (Thomas et al. 2011), whereby we will be able to analyze the interaction of the receding photosphere with the emerging glowing core of  $^{56}\text{Co}$  and its effects on the SN spectrum, a process which has so far received little attention.

The referee’s careful eye vastly improved the content of this work, for which we are grateful. This work was supported in part by NSF grant AST-0707704, and US DOE Grant DE-FG02-07ER41517, and by SFB 676, GRK 1354 from the DFG. Support for Program number HST-GO-12298.05-A was provided by NASA through a grant from the Space Telescope Science Institute, which is operated by the Association of Universities for Research in Astronomy, Incorporated, under NASA contract NAS5-26555. This research has made use of NASA’s Astrophysics Data System.

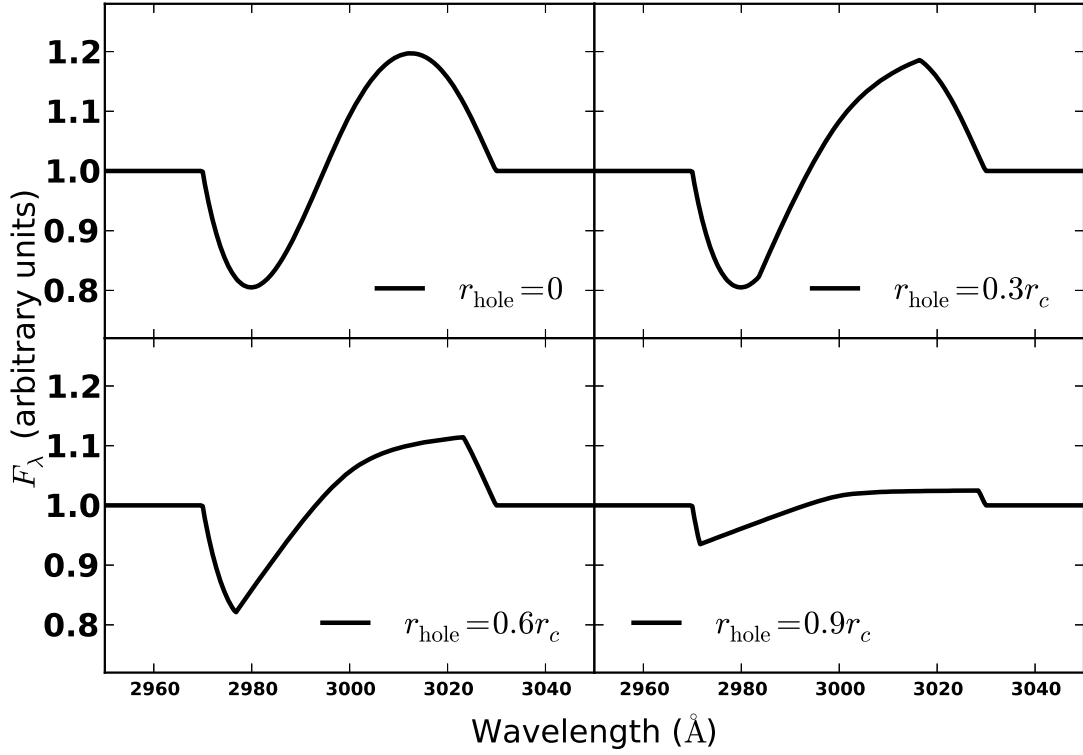


Fig. 15.— A post-photospheric line profile where the line is excluded from the various parts of the inner region of the core. The core has outer velocity  $3000 \text{ km s}^{-1}$ . The optical depth in the region  $r > r_{\text{hole}}$  is  $\tau = 1$ , whereas in  $r < r_{\text{hole}}$ ,  $\tau = 0$ . The rounded profile is replaced by a flattened profile, but there is still an emission peak and an absorption trough, both of which become more muted as  $r_{\text{hole}}$  increases.



## REFERENCES

- Axelrod, T. S. 1980, PhD thesis, California Univ., Santa Cruz.
- Bowers, E. et al. 1997, MNRAS, 290, 663
- Branch, D., Baron, E., Hall, N., Melakayil, M., & Parrent, J. 2005, PASP, 117, 545
- Branch, D., Doggett, J. B., Nomoto, K., & Thielemann, F.-K. 1985, ApJ, 294, 619
- Branch, D. et al. 1983, ApJ, 270, 123
- Castor, J. I. 1970, MNRAS, 149, 111
- De, S., Baron, E., & Hauschildt, P. H. 2010, MNRAS, 401, 2081
- Dessart, L. & Hillier, D. J. 2005, A&A, 437, 667
- Dessart, L. & Hillier, D. J. 2010, MNRAS, 405, 2141
- . 2011, MNRAS, 410, 1739
- Fesen, R. A., Höflich, P. A., Hamilton, A. J. S., Hammell, M. C., Gerardy, C. L., Khokhlov, A. M., & Wheeler, J. C. 2007, ApJ, 658, 396
- Fisher, A., Branch, D., Nugent, P., & Baron, E. 1997, ApJ, 481, L89
- Foley, R. J. & Kasen, D. 2011, ApJ, 729, 55
- Foley, R. J. et al. 2012, ApJ, 752, 101
- Gerardy, C. L. et al. 2007, ApJ, 661, 995
- Hachinger, S., Mazzali, P. A., & Benetti, S. 2006, MNRAS, 370, 299
- Hatano, K., Branch, D., Fisher, A., Baron, E., & Filippenko, A. V. 1999a, ApJ, 525, 881
- Hatano, K., Branch, D., Fisher, A., Deaton, J., & Baron, E. 1999b, ApJS, 121, 233
- Hillier, D. J. & Dessart, L. 2012, MNRAS, 424, 252
- Höflich, P. 2003, in Astronomical Society of the Pacific Conference Series, Vol. 288, Stellar Atmosphere Modeling, ed. I. Hubeny, D. Mihalas, & K. Werner (San Francisco: ASP), 185
- Höflich, P., Gerardy, C. L., Nomoto, K., Motohara, K., Fesen, R. A., Maeda, K., Ohkubo, T., & Tominaga, N. 2004, ApJ, 617, 1258
- Jack, D., Hauschildt, P. H., & Baron, E. 2009, A&A, 502, 1043

- Jeffery, D. & Branch, D. 1990, in *Supernovae*, ed. J. C. Wheeler & T. Piran (Singapore: World Scientific), 149
- Jeffery, D., Leibundgut, B., Kirshner, R. P., Benetti, S., Branch, D., & Sonneborn, G. 1992, *ApJ*, 397, 304
- Jeffery, D. J., Ketchum, W., Branch, D., Baron, E., Elmhamdi, A., & Danziger, I. J. 2007, *ApJS*, 171, 493
- Jerkstrand, A., Fransson, C., & Kozma, C. 2011, *A&A*, 530, A45
- Kasen, D., Thomas, R. C., & Nugent, P. 2006, *ApJ*, 651, 366
- Kozma, C. & Fransson, C. 1998a, *ApJ*, 496, 967
- . 1998b, *ApJ*, 497, 431
- Kromer, M. & Sim, S. A. 2009, *MNRAS*, 398, 1809
- Maeda, K., Benetti, S., Stritzinger, M., Röpke, F. K., Folatelli, G., Sollerman, J., Taubenberger, S., Nomoto, K., Leloudas, G., Hamuy, M., Tanaka, M., Mazzali, P. A., & Elias-Rosa, N. 2010, *Nature*, 466, 82
- Maeda, K., Leloudas, G., Taubenberger, S., Stritzinger, M., Sollerman, J., Elias-Rosa, N., Benetti, S., Hamuy, M., Folatelli, G., & Mazzali, P. A. 2011, *MNRAS*, 413, 3075
- Maeda, K., Nomoto, K., Mazzali, P. A., & Deng, J. 2006, *ApJ*, 640, 854
- Maund, J. R., Höflich, P. A., Patat, F., Wheeler, J. C., Zelaya, P., Baade, D., Wang, L., Clocchiatti, A., & Quinn, J. 2010, *ApJ*, 725, L167
- Maurer, I., Jerkstrand, A., Mazzali, P. A., Taubenberger, S., Hachinger, S., Kromer, M., Sim, S., & Hillebrandt, W. 2011, *MNRAS*, 418, 1517
- Mazzali, P. 2001, *MNRAS*, 321, 341
- Mazzali, P., Cappellaro, E., Danziger, I., Turatto, M., & Benetti, S. 1998, *ApJ*, 499, L49
- Mazzali, P., Danziger, I. J., & Turatto, M. 1995, *A&A*, 297, 509
- Mazzali, P. et al. 2005, *ApJ*, 623, L37
- Mazzali, P. A. 2000, *A&A*, 363, 705
- Mazzali, P. A., Chugai, N., Turatto, M., Lucy, L. B., Danziger, I. J., Cappellaro, E., della Valle, M., & Benetti, S. 1997, *MNRAS*, 284, 151
- Mazzali, P. A. & Lucy, L. B. 1993, *A&A*, 279, 447

- Mazzali, P. A., Maurer, I., Stritzinger, M., Taubenberger, S., Benetti, S., & Hachinger, S. 2011, MNRAS, 416, 881
- Mihalas, D. 1978, Stellar Atmospheres (New York: W. H. Freeman)
- Motohara, K., Maeda, K., Gerardy, C. L., Nomoto, K., Tanaka, M., Tominaga, N., Ohkubo, T., Mazzali, P. A., Fesen, R. A., Höflich, P., & Wheeler, J. C. 2006, ApJ, 652, L101
- Pinto, P. A. & Eastman, R. G. 2000, ApJ, 530, 757
- Ruiz-Lapuente, P. & Lucy, L. B. 1992, ApJ, 400, 127
- Thomas, R. C., Nugent, P. E., & Meza, J. C. 2011, PASP, 123, 237

### A. $S(r)$ outside the core

In §4 we calculate sample spectra for lines forming outside the glowing core. Therefore, we calculate the source function in the region  $r > r_c$ . From Figure 16:

$$Y = r\mu - (r^2\mu^2 + r_c^2 - r^2)^{1/2}.$$

Then

$$X = (X + Y) - Y = 2(r^2\mu^2 + r_c^2 - r^2)^{1/2}. \quad (\text{A1})$$

We plug the expression for  $X$  into Equation 5, noting that, because the shell emits no continuum, the maximum value of  $\theta$  is not 1, as in the  $r \leq r_c$  case, but rather

$$\theta_{\max} = \cos^{-1} \left( \frac{(r^2 - r_c^2)^{1/2}}{r} \right).$$

Thus,

$$J(r) = \frac{1}{2} \int_{\mu_0}^1 2(r^2\mu^2 + r_c^2 - r^2)^{1/2} d\mu,$$

where  $\mu_0$  is the argument of the inverse cosine above. The result is

$$\begin{aligned} J(r) &= \frac{1}{2r} \left\{ rr_c + (r^2 - r_c^2) \ln \left[ \frac{\sqrt{r^2 - r_c^2}}{r + r_c} \right] \right\} \\ &= \frac{1}{2r} \left\{ rr_c + \frac{(r^2 - r_c^2)}{2} \ln \left[ \frac{r - r_c}{r + r_c} \right] \right\}. \end{aligned} \quad (\text{A2})$$

The mean intensities inside and outside the core are identical except for two sign differences: one in the factor multiplying the logarithm, and the other in the argument of the logarithm itself. We find that Eqs. 7 and 8 are continuous at the edge of the core, as they must be, each yielding  $J(r = r_c) = 0.5r_c$ .

## B. Two lines

We now turn to the two-line case. We denote these lines as  $R$  and  $B$ , for “red” and “blue.” First, as stated previously, the source function for the blue line,  $S_B$ , is given by Equation 7. The source function for the red line,  $S_R(r)$ , is equal to the mean intensity  $J_\lambda(r)$ , where  $\lambda$  is the rest wavelength of the line  $\lambda_{0R}$ . The calculation of  $J$  is complicated by the fact that photons emitted by the blue line may be scattered into resonance with the red line, while some continuum photons from the glowing core which would, in the absence of the blue line, redshift into resonance with the red line are actually scattered away by the blue line. In velocity space the region where the blue line interacts with the red line takes the form of a “scattering sphere” called the *common point velocity surface* (CPVS) (Jeffery & Branch 1990). The radius of the CPVS, denoted  $Y$  in Figure 17, is given by the Doppler formula, Equation 14, where one replaces  $z$  in that equation with  $Y$ . In §B.1 we study the interaction of two lines confined to the core, and in §B.2 we explore two lines in the shell.

### B.1. Two lines inside the core

When both lines are confined to the core,  $S_R$  contains three components:

1. the intensity of continuum photons which can redshift into resonance with  $R$ , but are scattered away when they reach the CPVS;
2. photons emitted by  $B$  along the CPVS which redshift into resonance with  $R$ ;
3. continuum photons which form *inside* the CPVS and therefore redshift into resonance with  $R$  without interacting with  $B$ .

Segments 1 and 3 are labeled  $X$  and  $Y$  respectively in Figure 17. Mathematically we write this as

$$S_R = \frac{1}{2} \int_{-1}^1 X e^{-\tau_B} d\mu + \frac{1}{2} \int_{-1}^1 S_B (1 - e^{-\tau_B}) d\mu + \frac{1}{2} \int_{-1}^1 Y d\mu. \quad (\text{B1})$$

To calculate  $X = X(\mu)$  we refer to Figure 18. Defining the triangle  $ABC$  in Figure 18, we can use the law of cosines to find:

$$r_c^2 = (X + Y)^2 + r_R^2 - 2(X + Y)r_R\mu \quad (\text{B2})$$

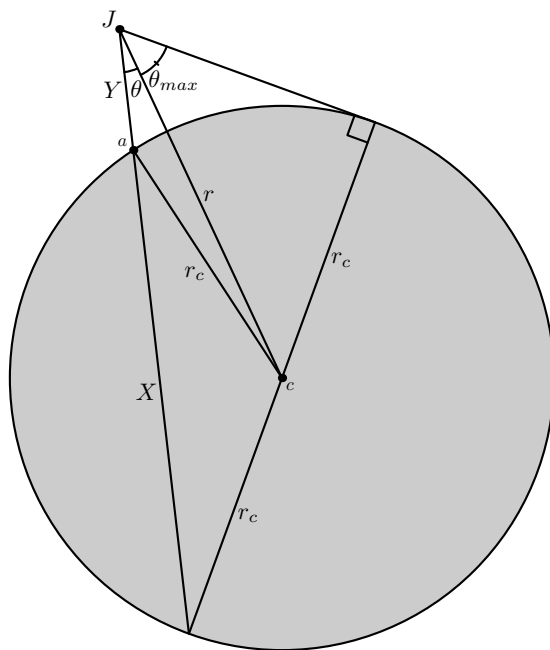


Fig. 16.— Geometric configuration used to calculate  $S(r > r_c)$  in the absence of lines in the core.

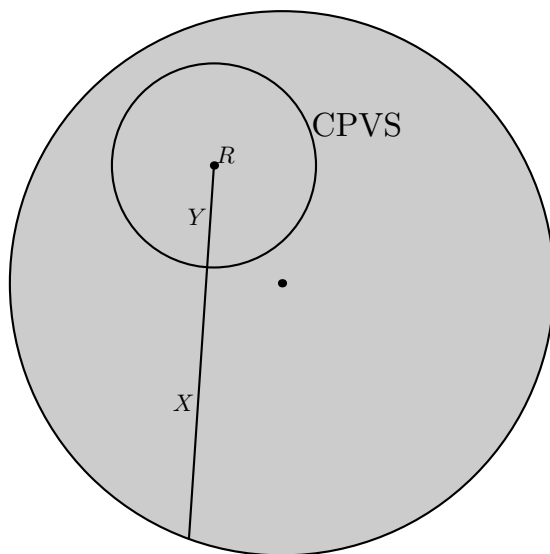


Fig. 17.— The different components of an intensity ray incident on the red line in the two-line case.

where we have used the fact that  $X$  and  $Y$  are co-linear and  $\mu = \cos \theta$ . Solving for  $X$ ,

$$X = (r_R \mu - Y) \pm \sqrt{(r_R \mu - Y)^2 + r_c^2 - r_R^2 + 2Y r_R \mu}. \quad (\text{B3})$$

Expanding the square root yields

$$\sqrt{(r_R \mu - Y)^2 + r_c^2 - r_R^2 + 2Y r_R \mu} = \sqrt{r_c^2 - r_R^2(1 - \mu^2) + Y^2}. \quad (\text{B4})$$

When  $-1 \leq \mu \leq Y/r_R$ , we see that  $(r_R \mu - Y) < 0$  and we must take the positive root in Equation B3. However, when  $Y/r_R < \mu \leq 1$  we see from Equation B3 that  $\mu > 0$  and thus the term in the square root is larger than the expression  $r_R \mu - Y$  and so the positive root is also correct. Hence,

$$X = (r_R \mu - Y) + \sqrt{r_c^2 - r_R^2(1 - \mu^2) + Y^2}, \quad (\text{B5})$$

for  $-1 \leq \mu \leq 1$ . Before proceeding we note that if the CPVS extends past the edge of the core, that is, if  $r_R + Y > r_c$ , then there exists a critical angle  $\theta_{\text{crit}}$  for which  $X$  becomes undefined if  $\theta > \theta_{\text{crit}}$ . Its value is

$$\mu_{\text{crit}} = \frac{Y^2 + r_R^2 - 1}{2Y r_R}, \quad (\text{B6})$$

where  $\mu_{\text{crit}} \equiv \cos \theta_{\text{crit}}$ . When integrating to find the contribution of the CPVS to the source function of the red line,  $S_R$ , we must stop the integration at this angle. This limit is depicted in Figure 19.

Next, we must calculate  $r_{S_B} = r_{S_B}(\mu)$ , the location of the CPVS, as shown in Figure 20. Again through vector addition arguments we find

$$r_{S_B}(\mu) = (r_R^2 + Y^2 - 2r_R Y \mu)^{1/2}. \quad (\text{B7})$$

It is at this location  $r_{S_B}$  that both  $\tau_B$  and  $S_B$  in Equation B1 are evaluated. Lastly we turn to the calculation of  $Y$  in Figure 17. If the entire CPVS fits inside the core, we may use the Doppler formula, Equation 14, to calculate  $Y$  for all  $\theta$ . However, if part of the CPVS extends past the edge of the core then  $Y$  takes a slightly more complicated form. This latter case is shown in Figure 21, where  $\theta_1 > \theta_{\text{crit}}$ . We calculated this angle in Equation B6. If  $\theta > \theta_{\text{crit}}$  then, from Figure 21,

$$D(\mu) = r_R \mu \pm (r_R^2 \mu^2 + r_c^2 - r_R^2)^{1/2}. \quad (\text{B8})$$

Since  $D$  is a length and must always satisfy  $D \geq 0$  we can rule out immediately the “minus” solution, since it is negative for all possible values of  $(r_R, Y, \mu)$ . Thus we take the positive root:

$$D(\mu) = r_R \mu + (r_R^2 \mu^2 + r_c^2 - r_R^2)^{1/2} \quad -1 \leq \mu \leq \mu_{\text{crit}}. \quad (\text{B9})$$

## B.2. Two lines outside the core

In the case that we have a resonance line that is strong under cold conditions, for example, certain lines of Ca II or Mg II, we may want to consider multiple lines forming outside the core.

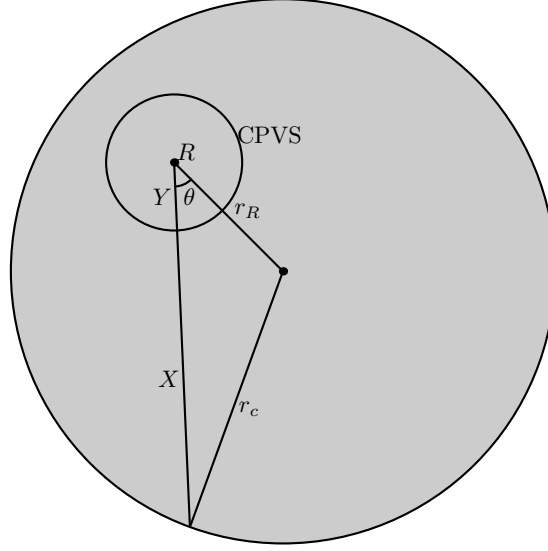


Fig. 18.— Explicit geometric construction of two-line configuration used to calculate  $X = X(\mu)$ .

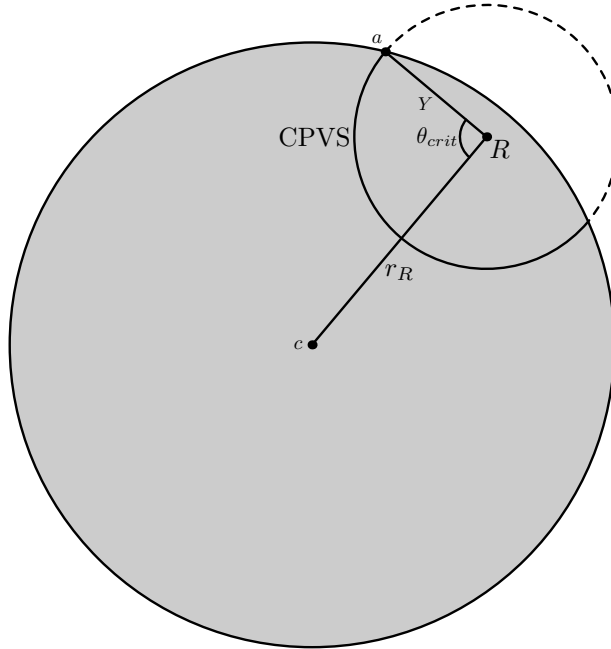


Fig. 19.— Geometric construction of angle  $\theta_{crit}$ . The value  $r_R$  is the magnitude of the vector  $\vec{cR}$ , and  $Y$  is that of  $\vec{aR}$ .

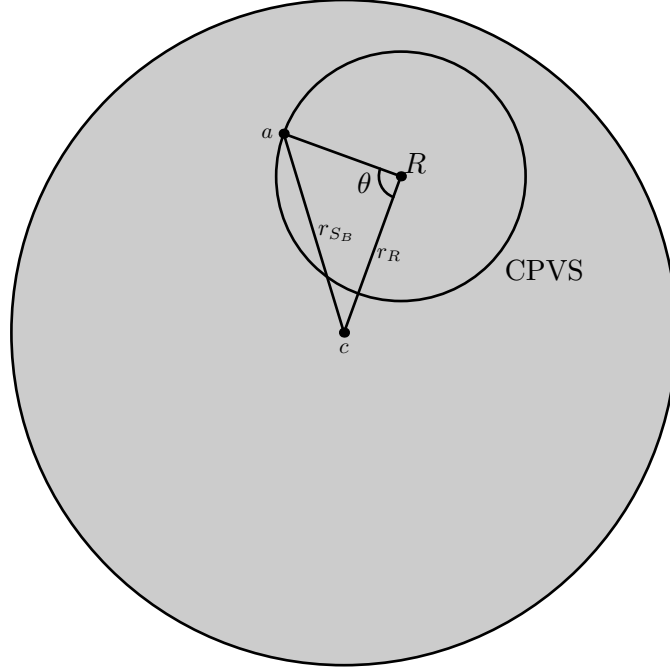


Fig. 20.— Calculation of location of CPVS, labeled  $r_{SB}$ , with respect to the center of the SN. The quantity  $r_R$  is the magnitude of the vector  $\vec{cR}$ , and  $r_{SB}$  is that of  $\vec{ac}$ .

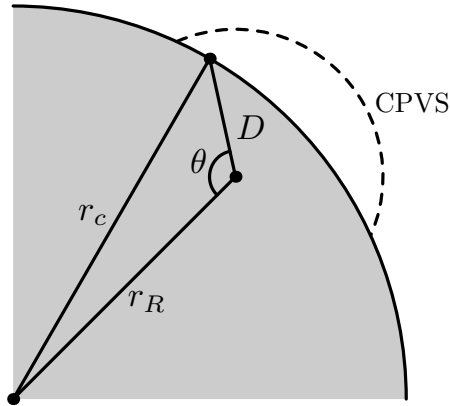


Fig. 21.— Geometric configuration of truncated intensity ray  $D = D(\mu)$ .



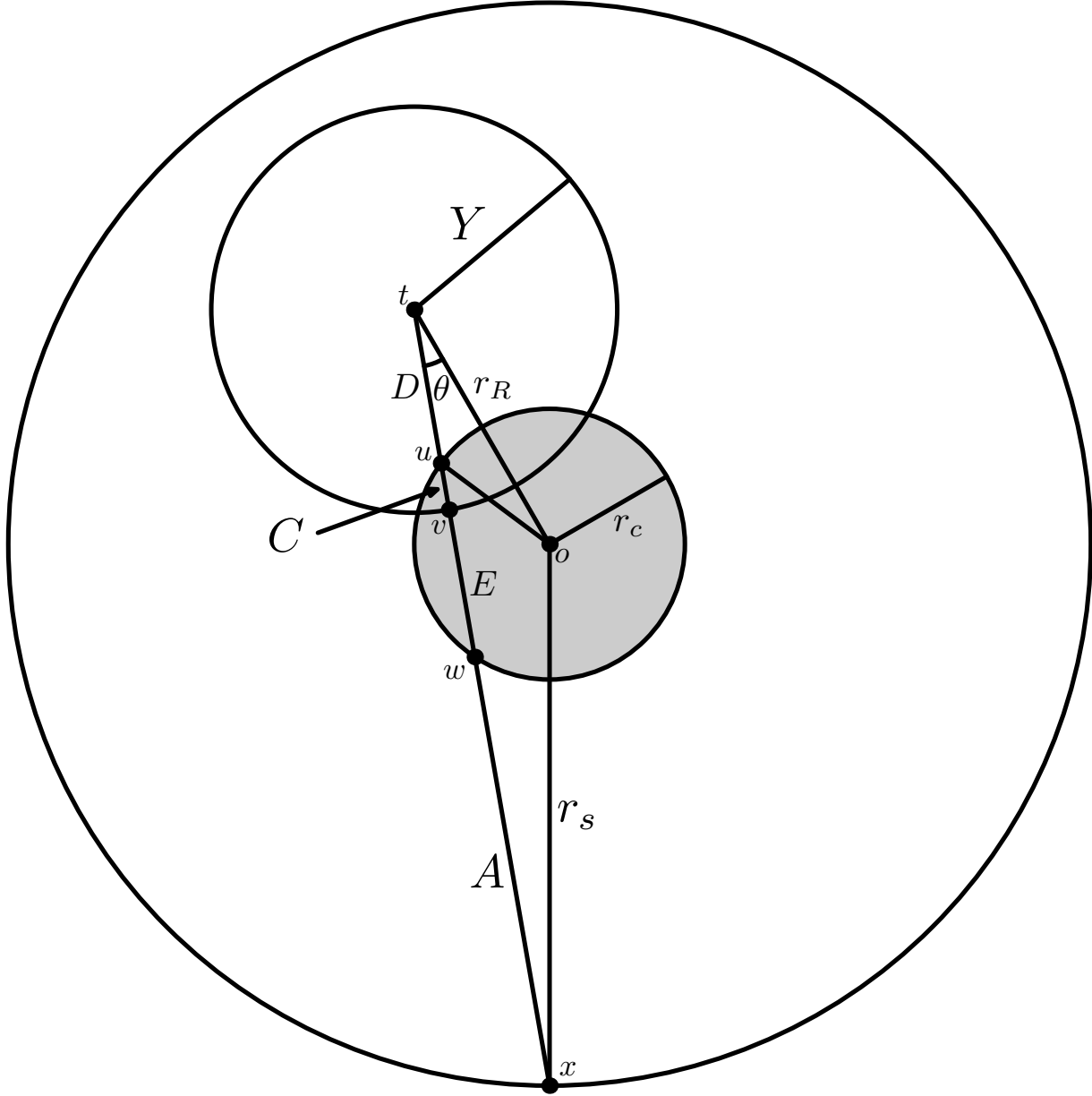


Fig. 22.— Case I geometry. The value of  $A$  corresponds to the magnitude of the vector  $\vec{xw}$ ,  $E$  to  $\vec{ow}$ ,  $C$  to  $\vec{ov}$ ,  $D$  to  $\vec{vt}$ ,  $r_c$  to  $\vec{oo}$ , and  $r_s$  to  $\vec{xo}$ . Only  $E$  and  $C$  contribute to the intensity of the ray since  $A$  and  $D$  lie outside the emitting core.

Figure 22 illustrates the most complex case. If  $\theta > \theta_{\text{crit}}$ , where  $\mu_{\text{crit}} = \cos(\theta_{\text{crit}}) = 1 - (r_c/r_R)^2$ , then the characteristic in that direction does not intersect the core and accumulates no intensity, but for the case that  $\mu \geq \mu_{\text{crit}}$  then the characteristic is given as shown in Cases I–III, (Figures 22–24).

For Case I, Figure 22, we find

$$D = r_R \cos \theta - \sqrt{r_c^2 - r_R^2 \sin^2 \theta}, \quad (\text{B10})$$

$$C = Y - D = Y - r_R \cos \theta + \sqrt{r_c^2 - r_R^2 \sin^2 \theta}, \quad (\text{B11})$$

$$E = 2(r_R \cos \theta - D) - C = \sqrt{r_c^2 - r_R^2 \sin^2 \theta} - Y + r_R \cos \theta, \quad (\text{B12})$$

and

$$A = \sqrt{r_s^2 - r_R^2 \sin^2 \theta} - \sqrt{r_c^2 - r_R^2 \sin^2 \theta}. \quad (\text{B13})$$

For Case II, Figure 23, we have

$$E = 2\sqrt{r_c^2 - r_R^2 \sin^2 \theta} \quad (\text{B14})$$

$$C = r_R \cos \theta - Y - \sqrt{r_c^2 - r_R^2 \sin^2 \theta} \quad (\text{B15})$$

$$A = \sqrt{r_s^2 - r_R^2 \sin^2 \theta} - \sqrt{r_c^2 - r_R^2 \sin^2 \theta} \quad (\text{B16})$$

and

$$D = Y. \quad (\text{B17})$$

For Case III, Figure 24,

$$D = r_R \cos \theta - \sqrt{r_c^2 - r_R^2 \sin^2 \theta} \quad (\text{B18})$$

$$C = 2\sqrt{r_c^2 - r_R^2 \sin^2 \theta} \quad (\text{B19})$$

$$E = Y - D - C = Y - \sqrt{r_c^2 - r_R^2 \sin^2 \theta} - r_R \cos \theta. \quad (\text{B20})$$

and

$$A = \sqrt{r_s^2 - r_R^2 \sin^2 \theta} + r_R \cos \theta - Y. \quad (\text{B21})$$

Then  $J$  for Case I is:

$$J = \frac{1}{2} \left\{ \int_{-1}^{\mu_{\text{crit}}} S_B(1 - e^{-\tau_B}) d\mu + \int_{\mu_{\text{crit}}}^1 [Ee^{-\tau_B} + S_B(1 - e^{-\tau_B}) + C] d\mu \right\}. \quad (\text{B22})$$

For Case II,  $J$  is:

$$J = \frac{1}{2} \left\{ \int_{-1}^{\mu_{\text{crit}}} S_B(1 - e^{-\tau_B}) d\mu + \int_{\mu_{\text{crit}}}^1 [Ee^{-\tau_B} + S_B(1 - e^{-\tau_B})] d\mu \right\}. \quad (\text{B23})$$

Finally, for Case III,

$$J = \frac{1}{2} \left\{ \int_{-1}^{\mu_{\text{crit}}} S_B(1 - e^{-\tau_B}) d\mu + \int_{\mu_{\text{crit}}}^1 [E + S_B(1 - e^{-\tau_B})] d\mu \right\} \quad (\text{B24})$$

The extension of the two-line case to the  $N$ -line case is straightforward and is implemented most easily in a recursive fashion, moving along wavelength as the value of  $r_R$  increases.

Fig. 23.— Case II geometry. The value of  $A$  corresponds to the magnitude of the vector  $\overrightarrow{xw}$ ,  $E$  to  $\overrightarrow{wu}$ ,  $C$  to  $\overrightarrow{uw}$ ,  $D$  to  $\overrightarrow{ut}$ ,  $r_c$  to  $\overrightarrow{ou}$ , and  $r_s$  to  $\overrightarrow{ox}$ . Only  $E$  contributes to the intensity of the ray since  $A$ ,  $C$ , and  $D$  lie outside the emitting core.

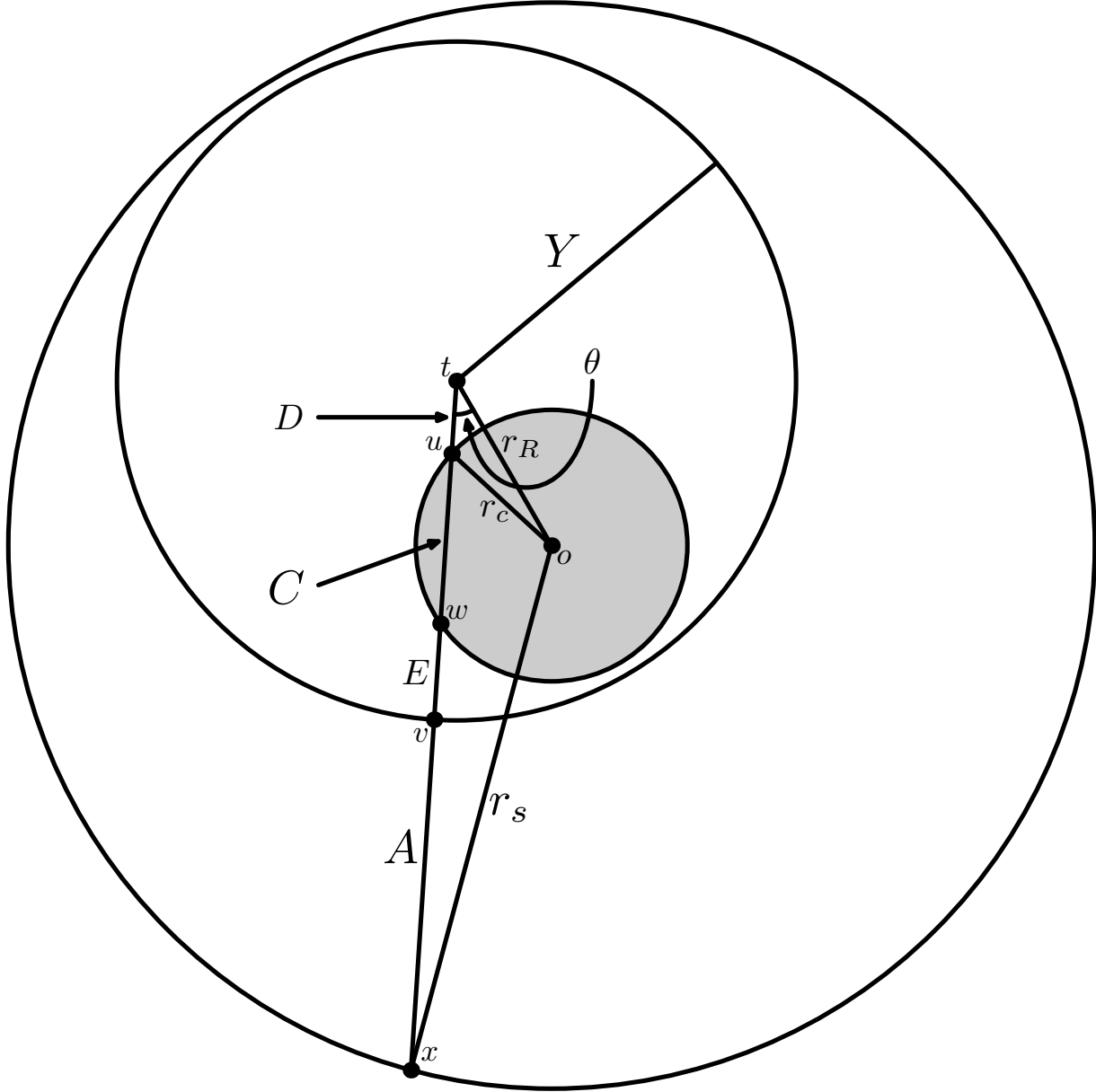


Fig. 24.— Case III geometry. The value of  $A$  corresponds to the magnitude of the vector  $\vec{x}\vec{o}$ ,  $E$  to  $\vec{v}\vec{u}$ ,  $C$  to  $\vec{w}\vec{u}$ ,  $D$  to  $\vec{u}\vec{t}$ ,  $r_c$  to  $\vec{o}\vec{u}$ , and  $r_s$  to  $\vec{x}\vec{o}$ . Only  $C$  contributes to the intensity of the ray since  $A$ ,  $E$ , and  $D$  lie outside the emitting core.

### B.3. Calculation of emergent intensity

Given that the flux integral in Equation 4 can be written as an integral over impact parameter  $p$ , we concern ourselves here with the calculation of the emergent intensity of rays with constant  $p$ , denoted  $I_\lambda(p)$ . We first calculate the domain  $[z_{\min}, z_{\max}]$  over which a ray with given  $p$  exists:

$$\begin{aligned} z_{\min} &= -(r_c^2 - p^2)^{1/2} \\ z_{\max} &= +(r_c^2 - p^2)^{1/2} \end{aligned}$$

We then use the Doppler formula to establish the wavelength domain  $[\lambda_{\min}, \lambda_{\max}]$  over which it is possible for a particular wavelength point  $\lambda$  to be in resonance in the core, given  $p$ :

$$\lambda_{\min} = \frac{\lambda}{1 + z_{\max} \left( \frac{v_{\text{core}}}{c} \right)} \quad (\text{B25})$$

$$\lambda_{\max} = \frac{\lambda}{1 + z_{\min} \left( \frac{v_{\text{core}}}{c} \right)}. \quad (\text{B26})$$

All lines with rest wavelength  $\lambda_0$  which lie in this domain will be in resonance with the ray  $I_\lambda(p)$  at some location in the core.

Now consider a ray with two lines which both fall in the domain  $[\lambda_{\min}, \lambda_{\max}]$ . The ray redshifts into resonance with the blue line “before” (at larger  $z$ , closer to the back of the core) redshifting into resonance with the red line; we denote these locations  $z_B$  and  $z_R$ , respectively, where  $z_B > z_R$ . The segment of the ray between the back edge of the core and  $z_B$  has intensity  $(r_c^2 - p^2)^{1/2} - z_B$ . However it will redshift into resonance with *both* lines before emerging from the core, so it acquires two attenuation terms,  $e^{-\tau_B}$  and  $e^{-\tau_R}$ , where  $\tau_B$  and  $\tau_R$  are evaluated at  $z_B$  and  $z_R$ , respectively. The continuum segment between  $z_R$  and  $z_B$  has length  $z_B - z_R$  and is attenuated only by the red line. The front-most continuum piece, between  $z_R$  and the front of the core, is unaffected by scattering and has intensity  $(r_c^2 - p^2)^{1/2} + z_R$ .

The source functions of the red and blue lines also contribute to the total emergent intensity. The contribution from each is  $S_i(1 - e^{-\tau_i})$ , where  $i \in \{R, B\}$ . However the blue line’s contribution will be attenuated when it redshifts into resonance with the red line, and so it receives the usual  $e^{-\tau_R}$  multiplicative factor. Therefore the total emergent intensity is

$$\begin{aligned} I_\lambda(p) &= ((r_c^2 - p^2)^{1/2} - z_B)e^{-\tau_B}e^{-\tau_R} + S_B(1 - e^{-\tau_B})e^{-\tau_R} + (z_B - z_R)e^{-\tau_R} \\ &\quad + S_R(1 - e^{-\tau_R}) + (r_c^2 - p^2)^{1/2} + z_R. \end{aligned} \quad (\text{B27})$$

If for a particular ray one of the two lines is outside  $[\lambda_{\min}, \lambda_{\max}]$ , the result for  $I_\lambda(p)$  reduces to the one-line form for  $I_\lambda(p)$  of Equation 10 or Eqs. 15, 17, and 18 for lines outside the core. It is important to understand that if, for some impact parameter  $p$ , the blue line has wavelength outside  $[\lambda_{\min}, \lambda_{\max}]$ , such that  $I_\lambda(p)$  is given by Equation 10, the source function  $S = S_R$  evaluated in that equation may nevertheless contain scattering effects of the blue line, as long as at least some portion of the CPVS for the blue line lies within the core.

If both lines fall outside this domain the emergent intensity becomes the pure continuum result.